

1 **Myosin II isoforms play distinct roles in *adherens* junction biogenesis**

2
3
4
5
6
7
8
9
10
11
12
13
14
15
16
17
18
19
20
21
22
23
24
25
26
27
28

Mélina L. Heuzé^{1§*}, Gautham Sankara^{1§}, Tien Dang¹, Joseph d'Alessandro¹, Victor Cellerin¹
David S. Williams², Jan C. M. van Hest³, Philippe Marcq⁴, René-Marc Mège^{1*}, Benoît Ladoux^{1*}.

¹ Institut Jacques Monod, CNRS UMR 7592, Université Paris Diderot, Paris, France.

² Department of Chemistry, College of Science, Swansea University, Swansea, UK.

³ Eindhoven University of Technology, Institute for Complex Molecular Systems, Eindhoven
The Netherlands.

⁴ Laboratoire Physique et Mécanique des Milieux Hétérogènes, CNRS UMR 7636, Sorbonne
Université, Paris, France.

§ These authors contributed equally to the work.

* Co-corresponding authors.

29 **Abstract**

30 Adherens junction (AJ) assembly under force is essential for many biological processes like
31 epithelial monolayer bending, collective cell migration, cell extrusion and wound healing. The
32 acto-myosin cytoskeleton acts as a major force-generator during the *de novo* formation and
33 remodelling of AJ. Here, we investigated the role of myosinII isoforms in epithelial junction
34 assembly. Myosin IIA (NMIIA) and Myosin IIB (NMIIB) differentially regulate biogenesis of
35 adherens junction through association with distinct actin networks. Analysis of junction
36 dynamics, actin organization, and mechanical forces of control and knockdown cells for
37 myosins revealed that NMIIA provides the mechanical tugging force necessary for cell-cell
38 junction reinforcement and maintenance. NMIIB is involved in E-cadherin clustering,
39 maintenance of a branched actin layer connecting E-cadherin complexes and perijunctional
40 actin fibres leading to the building-up of anisotropic stress. These data reveal unanticipated
41 complementary functions of NMIIA and NMIIB in the biogenesis and integrity of AJ.

42

43 **Introduction**

44 Tissue integrity and plasticity rely on cell-cell adhesion and cell contractility. The formation,
45 remodelling and disassembly of cell-cell adhesions are fundamental events accompanying all
46 stages of morphogenesis, tissue homeostasis and healing. *Adherens* junctions (AJ) mediated
47 by E-cadherin/catenin complexes are key elements of epithelial cell-cell adhesions and the
48 first ones to assemble upon contact initiation¹⁻³. They provide strong mechanical coupling
49 between neighbouring cells through association with the acto-myosin cytoskeleton⁴.

50 The assembly of *de novo* AJ is crucial for cell-cell rearrangement^{5,6}, tissue closure⁷ and the
51 maintenance of epithelial cell integrity during wound healing or cell extrusion⁸⁻¹⁰. During *de*
52 *novo* cell-cell contacts formation, initial contacts between facing lamellipodia induce immediate
53 clustering of cadherin molecules by trans- and cis-oligomerization¹¹⁻¹⁴. Subsequent signalling
54 events involving RhoGTPases trigger local remodelling of the actin cytoskeleton through
55 Arp2/3- or formin-mediated actin polarization in the vicinity of AJs¹⁵⁻¹⁷. These cytoskeletal
56 rearrangements drive the expansion of cell-cell contacts and inter-cellular adhesion

57 strengthening^{2,18,19}.

58 Non-muscle Myosin II (NMII) has emerged as a fundamental player in force-generation and
59 force-transmission at AJ both *in vitro* and *in vivo*^{20–22}. NMII is essential for epithelial tissue
60 architecture²³, epithelial tissue morphogenesis²⁴, tissue repair^{25,26} and cell extrusion²⁷. NMII
61 protects junctions from disassembly during development²⁸ and provides the mechanical
62 tugging force necessary for AJ reinforcement²⁹. In endothelial cells, NMII is recruited early in
63 filopodia-mediated bridge bundles and its activity is required for accumulation of VE-cadherin
64 in nascent AJs³⁰. In epithelial cells, NMII favours local concentration of E-cadherin at cell-cell
65 contacts^{31,32} and it is enriched at the edges of elongating junctions where it drives contact
66 expansion in response to RhoA activity^{17,18}.

67 In mammalian cells, NMII heavy chains exist as three different isoforms: NMIIA, NMIIB and
68 NMIIC encoded by *MYH9*, *MYH10* and *MYH14* genes respectively^{33,34}. NMIIA and NMIIB are
69 widely expressed whereas NMIIC is not detected in several tissues³⁵. Despite structural
70 similarities, NMIIA and NMIIB isoforms have been assigned both redundant and specific
71 functions depending on cell types and processes³⁶. NMIIA and NMIIB exhibit different ATPase
72 activities and actin-binding properties^{37–40}, in addition to their specific C-terminal tails that
73 confer them unique functions^{41–43}. These two isoforms can exist as activated monomers in
74 cells, but they can also co-assemble as homotypic and heterotypic filaments^{44,45}. NMIIA and
75 NMIIB play both unique and overlapping roles *in vivo*^{46–51}. In cells migrating on 2D surfaces,
76 NMIIA localizes at the cell front, limits lamellipodial protrusive activity and reduces 2D cell
77 migration speed by regulating focal adhesions dynamics and traction forces^{52–55}. NMIIB
78 localizes at the cell rear and is required for front-back polarity and tail retraction^{53–61}. In 3D,
79 NMIIA favours cell displacement^{52–55,62} while NMIIB drives nuclear translocation⁶³. NMIIB also
80 plays a determinant role in durotaxis⁶⁴.

81 While the roles of NMII isoforms in cell motility on ECM have been extensively studied, very
82 little is known on their respective functions in AJs organization. Smutny and collaborators have
83 reported that NMIIA and NMIIB both localize at apical junction complexes of polarized MCF-7
84 cells. Upon specific isoform expression silencing, they further proposed that NMIIA may favour

85 the accumulation of E-cadherin in the AJ belt while NMIIB may stabilize the associated
86 perijunctional actin ring³². Efimora and collaborators reported an association of NMIIA with
87 contractile actin bundle running parallel to linear AJ in endothelial cells, but failed to precisely
88 localize NMIIB⁶⁵. Here we questioned the unexplored functions of NMII isoforms in epithelial
89 AJ biogenesis using an *in vitro* system based on chemically-switchable micro-patterns,
90 whereby we can control the time and location of a new contact forming between two single
91 cells on a matrix-coated surface.

92

93 **Results**

94 ***In vitro* system for the study of early cell-cell contacts**

95 In order to study early AJ biogenesis, pairs of GFP-E-cadherin expressing MDCK cells were
96 plated on arrays of 5 μm -distant fibronectin-coated micro-patterns surrounded by switchable
97 cytopulsive surfaces⁶⁶. After complete spreading, the confinement imposed by the micro-
98 patterns was released by addition of an RGD-motif containing modified peptide that switched
99 the surface surrounding patterns from a cytopulsive to an adhesive surface (Supplementary
100 Fig. 1a). Junction biogenesis was monitored by confocal spinning disk microscopy (Fig. 1a,
101 Supplementary Video 1). Within 2 hours, cells extended lamellipodia in random directions and
102 approximately 50 % of the pairs of cells contacted within 12 hours. The junction extended
103 reaching a plateau at 40-45 μm length in around 3 hours (Fig. 1b,d). As previously described¹⁷,
104 GFP-E-cadherin accumulated at the edges of the junction (Fig. 1b). Once reaching this
105 maximal length, the junction was maintained while showing dynamic retraction-elongation
106 events (Fig. 1b). Importantly, in 98 +/- 2 % of the cases, cell-cell contacts were stable and
107 lasted above 3 hours and up to 22 hours (Fig. 1b,e). Analysis of the nucleus-centrosome axis
108 relative to the junction axis showed a relocalization of the centrosome towards the lamellipodia
109 opposite to the cell-cell contact within one hour (Supplementary Fig. 1b,c), as previously
110 reported in different systems and cell types⁶⁷⁻⁷⁰. However, although MDCK cells antipolarized
111 in the doublet as if they were initiating a contact inhibition of locomotion, they remained
112 attached to each other in contrast to more mesenchymal cells that proceed with cell separation

113 following repolarization⁷¹. Together, these observations show that this *in vitro* model system is
114 suitable for the study of early cell-cell contacts at high spatial-temporal resolution.

115

116 **NMIIA and NMIIB orchestrate junction biogenesis**

117 To evaluate the involvement of NMII-generated actomyosin contractility in junction biogenesis,
118 we monitored junction formation in cells treated with the ROCK inhibitor Y27632
119 (Supplementary Video 2). Y27-treated cells exhibited irregular junctions with small digitations
120 and empty spaces and did not elongate as much as in control cells (Fig. 1c,d). They were
121 strongly affected in their capacity to maintain cell-cell contacts, half of the doublets separating
122 before 3 hours (Fig. 1e, f and Supplementary Video 2). Similar results were observed after
123 treating cells with the NMII ATPase activity inhibitor blebbistatin (data not shown) indicating
124 that NMII activity is required for proper junction elongation and stabilization. Furthermore, NMII
125 was required for the centrosome repolarization, as we could not observe any preferential
126 orientation of the nucleus-centrosome axis in Y27-treated doublets (Supplementary Fig. 1d).
127 Next, we explored the involvement of the two NMII isoforms in junction biogenesis. NMIIA has
128 been reported to be by large the major isoform of NMII expressed in MDCK cells³⁵. However,
129 immunostainings revealed that the three isoforms, NMIIA, NMIIB and NMIIIC could be detected
130 in MDCK cells. NMIIA and NMIIIC fully co-localized to similar structures, which was not the case
131 for NMIIB (Supplementary Fig. 3a,b). For these reasons, we decided to focus on NMIIA and
132 NMIIB isoforms. Expression of each isoform was silenced in GFP-E-cadherin MDCK cells by
133 stable transfection of specific ShRNA encoding plasmids, leading to an inhibition of expression
134 of around 60-70% (Fig. 2a,b and Supplementary Fig. 2a,b). The analysis of cell-cell contact
135 formation in cell doublets by live-imaging (Supplementary Video 3) revealed that NMIIB knock-
136 down (NMIIB KD) cells formed and extended intercellular junctions very similar to control (Ctrl)
137 cells (Fig. 2c-f). In contrast, almost half of NMIIA knock-down (NMIIA KD) cell doublets were
138 unable to sustain contacts more than 3 hours, and when they did so, these contacts remained
139 shorter than for Ctrl or NMIIB KD cell doublets (Fig. 2c-f), similar to what was observed in Y27-
140 treated cell doublets. NMIIB KD doublets, despite their ability to maintain cell-cell contacts for

141 longer times, formed twisted junctions that were significantly less straight than Ctrl and NMIIA
142 KD cells and deviated significantly more from their initial orientation (Fig. 2g,h). These defects
143 in NMIIB KD cells were already observed at early stages of junction biogenesis and were
144 associated to the formation of large extensions of junctional membrane (Fig.2i, arrows).
145 Together, these results show that both NMIIA and NMIIB are required for the biogenesis of
146 stable AJs, albeit with different contributions; NMIIA favours temporal stability whereas NMIIB
147 ensures the straightness and spatial stability of the junctions.

148

149 **NMIIB localizes to a junctional actin pool distinct from perijunctional NMIIA-associated** 150 **contractile fibres**

151 To better understand the respective roles of NMIIA and NMIIB in junction biogenesis, we next
152 studied their subcellular localization at nascent cell-cell contacts in cell doublets.
153 Immunostainings revealed that the localization of the two isoforms was mutually exclusive.
154 Anti-NMIIA antibodies stained actin bundles that were parallel to the junction but set at 1 to 2
155 μm from it. NMIIA was also found associated to actin cables parallel to the cortex of non-
156 junctional membranes (Fig. 3a,b,e and Supplementary Fig. 3a) in addition its association to
157 the classical ventral stress fibres. In contrast, NMIIB immunostaining was associated with the
158 junctional plasma membranes as well as with a cytoplasmic network (Fig. 3c-e and
159 Supplementary Fig. 3b), that was identified as the vimentin intermediate filament network as
160 reported by Menko and colleagues⁷² in lens epithelial cells. Importantly, the localization of
161 each isoform was not affected by the silencing of the other isoform (Supplementary Fig.3c).
162 Smutny and colleagues previously reported that NMIIA and NMIIB both localized to apical
163 epithelial junctions in polarized MCF-7 cells³². Given that, we followed the localization of both
164 isoforms during apico-basal polarization of MDCK cells (Fig. 3f and Supplementary Fig. 3d).
165 After 3 days of culture, confluent MDCK cells started to develop an apico-basal polarization
166 and the two isoforms colocalized to apically positioned *zonulae adherens* colocalizing with E-
167 cadherin as previously reported in MCF-7 cells³². At the ventral side, they were associated to
168 stress fibres. However, we confirmed a different localization of NMIIB and NMIIA in sub-

169 confluent cell clusters after one day of culture. NMIIA was still associated to stress fibres while
170 NMIIB colocalized with E-cadherin at cell-cell contacts. These differential distributions at the
171 early stages of AJ formation were not specific to MDCK cells, and were observed as well in
172 small clusters of Caco2 cells (Supplementary Fig.3e). Considering recent findings showing a
173 possible interaction between NMIIB and α -catenin⁷³, we hypothesized that NMIIB could be
174 recruited to the junction through α -catenin/E-cadherin complexes. Accordingly, in α -catenin KD
175 MDCK cells⁷⁴, NMIIB was relocalized to NMIIA-enriched stress fibres and circumnuclear actin
176 cables (Fig. 3e), indicating that α -catenin is required for NMIIB junctional recruitment.

177 To better characterize the organization of the actomyosin cytoskeleton at nascent AJs, co-
178 stainings of NMIIA, NMIIB, F-actin and β -catenin performed on control MDCK cells were
179 imaged using structured illumination microscopy (SIM). NMIIA was associated to thick F-actin
180 bundles running parallel to, and located a few microns away from the junctional membranes
181 (Fig. 4a), as reported for NMIIA localization in linear junctions of endothelial cells^{30,65}. We
182 confirmed at this resolution that NMIIA did not colocalize with β -catenin-labelled cadherin-
183 catenin complexes. Interestingly, NMIIA appeared distributed on these actomyosin bundles in
184 sarcomere like structures as described before in other cellular contexts^{75,76}. These NMIIA
185 labelled structures were almost free of NMIIB staining. NMIIB junctional staining colocalizing
186 with β -catenin was associated with a 200 nm to 1 μ m thick fuzzy F-actin network (Fig. 4a,b).
187 This junctional F-actin network was labelled by both Arp2/3 and cortactin (Fig. 5b,c) thus
188 corresponding to an Arp2/3-nucleated branched actin meshwork. Looking at short junctions
189 that probably corresponded to nascent cell-cell contacts, we could also observe the strong
190 enrichment of NMIIB and the exclusion of NMIIA at the contact zone (Fig.4c,d).

191 Altogether, these observations reveal that early during AJ biogenesis, NMIIB is exclusively
192 associated to a junctional Arp2/3-nucleated F-actin, structurally distinct from the perijunctional
193 contractile NMIIA-associated actin bundles running parallel to the junction.

194

195

196

197 **NMIIA regulates the organization of perijunctional actin bundles while NMIIB supports**
198 **the maintenance of the junctional branched actin layer**

199 Based on these observations, we subsequently explored the possibility that NMIIB and NMIIA
200 could differentially regulate actin assembly at the junction, thereby maintaining its structural
201 integrity. Using SIM microscopy, we analyzed the organization of junctional actin cytoskeleton
202 in NMIIA KD and NMIIB KD cells. NMIIA KD cells exhibited shorter actin bundles running
203 parallel to the junction, while their junctional F-actin meshwork was comparable to the one of
204 Ctrl cells, both in terms of morphology and cortactin staining (Fig. 5b,c and Supplementary Fig.
205 4). In contrast, NMIIB KD cells presented a strongly enlarged area of junctional F-actin
206 meshwork colocalizing with β -catenin that corresponded to overlapping membrane extensions
207 stained with cortactin (Fig.5b,c and Supplementary Fig.4). In addition, while they retained
208 some of the perijunctional actin bundles, we could observe numerous oblique actin bundles
209 directed toward the junction (Fig.5c and Supplementary Fig.4). These results show that NMIIA
210 supports the organization of perijunctional actin bundles while NMIIB is required for the
211 regulated assembly of junctional branched F-actin that couples perijunctional bundles to the
212 plasma membrane.

213 The Arp2/3-nucleated actin network at the *zonula adherens* has been shown to regulate
214 junctional tension in epithelial monolayers⁷⁷. On the other hand, junctional tension has been
215 shown to associate with the presence of α -catenin molecules under open conformations^{78,79}.
216 Moreover, a direct link between α -catenin and NMIIB has been reported⁷³, suggesting that
217 NMIIB recruitment, α -catenin molecular unfolding and regulation of Arp2/3-dependent
218 branched actin polymerization could be tightly linked. Thus, we performed immunostainings
219 with the α 18 monoclonal antibody recognizing the open conformation of the protein⁷⁹.
220 Strikingly, the ratio of α 18 on total α -catenin junctional staining was decreased by four times
221 in NMIIB KD cells compared to Ctrl cells, while it was not affected in NMIIA KD cells. This
222 suggests that junctional α -catenin molecules were significantly turned to the closed
223 conformational state in NMIIB KD cells (Fig.5d-f). In contrast, the total α -catenin junctional

224 levels were significantly reduced in NMIIA KD cells, as shown by others^{31,32}. Taken together,
225 these results strengthen complementary contributions for NMIIB and NMIIA where NMIIB is
226 the main isoform required for the organization of junctional branched actin and NMIIA for
227 organization of perijunctional contractile actin fibres.

228

229 **NMIIA is required for the generation of forces at E-cadherin adhesions while NMIIB**
230 **favours their transmission through F-actin anchoring**

231 The formation of cell-cell junctions in cell doublets is concomitant with the formation of cell-
232 matrix adhesions and the tugging force applied on cell-cell contacts must be compensated by
233 traction of the cells on cell-matrix adhesion complexes^{29,80-82}. To further understand the
234 contributions of NMII isoforms in junction biogenesis, we thus experimentally decoupled these
235 two adhesion systems. We first investigated the role of NMII isoforms in cell-matrix adhesion
236 by seeding single Ctrl, NMIIA KD and NMIIB KD cells on fibronectin-coated glass. NMIIA KD
237 cells spread 1.7 times more than Ctrl and NMIIB KD cells on fibronectin and their actin
238 cytoskeleton was highly perturbed exhibiting a strong decrease in ventral stress fibres and
239 cortical actin bundles together with an enlargement of their lamellipodia (Fig. 6a,b). NMIIA KD
240 cells also formed significantly less focal adhesions (Fig. 6a,c). In contrast, NMIIB KD cells
241 showed no defect in actin organization, cell spreading or focal adhesion formation (Fig. 6a-c).
242 Next, we measured by TFM the magnitude of traction forces applied by single cells on
243 deformable fibronectin-coated 30 kPa PDMS gels. NMIIA KD cells exerted lower traction forces
244 than Ctrl cells as reported by others^{55,61}. NMIIB KD cells, on the contrary, did not show any
245 defect in traction force generation on this substratum (Fig. 6d,e). These results, in agreement
246 with previous studies^{55,57}, show that NMIIA is the isoform regulating cell spreading, cell
247 adhesion, traction force generation and organization of contractile actin structures on
248 fibronectin. In contrary NMIIB is not contributing at all to the cell-matrix adhesion, focal
249 adhesion formation, actomyosin reorganization and traction forces on fibronectin.

250 To explore the contribution of NMII isoforms to E-cadherin-mediated cell-cell adhesion *per se*,
251 we seeded single cells on E-cadherin-coated substrates (Fig. 7a,b). After 6 hours, Ctrl and

252 NMIIA KD cells had spread similarly with mean areas of $1178 \pm 40 \mu\text{m}^2$ and $1031 \pm 37 \mu\text{m}^2$
253 respectively, while NMIIB KD cells spreading was significantly reduced (mean area = 515 ± 21
254 μm^2) (Fig. 7a,c). Ctrl cells organized thick circumnuclear actin arcs, as well as radial actin fibres
255 connected to peripheral β -catenin clusters (Fig. 7a), as previously described^{83,84}. NMIIA KD
256 cells, while spreading as Ctrl cells on E-cadherin and forming cadherin clusters in similar
257 numbers, lacked the circumnuclear actin arcs (Fig. 7a,c,d). In contrast, NMIIB KD cells kept
258 the organization of circumnuclear actin arcs, but were depleted of radial actin bundles, did not
259 form significant β -catenin clusters and failed to spread on E-cadherin (Fig. 7a,c,d). This data
260 indicated that NMIIB, but not NMIIA, plays a major role in the clustering and stabilization of E-
261 cadherin/catenin complexes that in turn promote cell spreading. Our findings also suggest that
262 NMIIA, but not NMIIB, is required for the formation of contractile actin fibres that apply traction
263 forces on the cadherin adhesions. We thus measured the capacity of these cells to transmit
264 forces through E-cadherin complexes by TFM, seeding them on E-cadherin-coated 15 kPa
265 PDMS elastic gels. Compared to Ctrl cells, NMIIA KD cells exhibited very low forces on E-
266 cadherin substrate (Fig.7e,f), confirming that NMIIA generates the forces transmitted to E-
267 cadherin adhesions. NMIIB KD cells, that failed to cluster cadherin/catenin complexes, also
268 generated lower traction forces than Ctrl cells, albeit to a lesser extent than NMIIA KD cells
269 (Fig. 7e, f). Even though both myosin isoforms contribute to cell-generated forces on E-
270 cadherin substratum, they have complementary contributions. NMIIA is required for the
271 formation of stress fibres while NMIIB would rather regulate the transmission of force and the
272 coupling of actin stress fibres to the cadherin-catenin complexes.

273

274 **NMIIA and NMIIB are required for proper organization of inter-cellular junctional stress**

275 To directly determine how NMIIA and NMIIB contribute to traction force generation and
276 transmission during AJ biogenesis, we mapped traction forces before and after cell-cell contact
277 formation in cell doublets. Hotspots of traction forces were generated at the periphery of the
278 doublet where lamellipodia arise (Fig.8a). As expected from the TFM data obtained with single
279 cells seeded on fibronectin, NMIIA KD doublets, compared to Ctrl and NMIIB KD ones,

280 exhibited very low traction forces both before and after cell-cell contact formation (Fig. 8a-c).
281 NMIIB KD doublets developed traction forces similar in magnitude to those developed by Ctrl
282 ones, with however different patterns. Hotspots of forces frequently appeared in the junctional
283 area in NMIIB KD doublets that were generally absent in Ctrl and NMIIA doublets (Fig. 8a). We
284 quantified these differences by analysing the spatial repartition of forces in the peripheral and
285 central subdomains of the junction, and their orientation relative to main junction axis (parallel,
286 $F_{//}$, and perpendicular, F_{\perp} , components). NMIIB KD doublets generated higher F_{\perp} in the central
287 part of the junction and lower values of $F_{//}$ (albeit not significantly) with respect to Ctrl doublets
288 in both the peripheral and the central part of the junction (Supplementary Fig.5a-c). These
289 results show that NMIIB plays an important role in the repartition of traction forces under the
290 junction and that NMIIA is essential for the generation of traction forces in general. We next
291 quantified the capacity of NMIIA KD and NMIIB KD cells to transmit forces across the junction.
292 Following Newton's laws, the net traction force exerted by an isolated doublet is zero, up to
293 the measurement noise. Conversely, the net traction forces exerted by each of the two cells
294 are equal in magnitude and opposite in direction, compensating exactly^{29,80,81}. We thus
295 calculated the resultant vectorial sum of forces per cell (Fig. 8b). In all conditions, the resultant
296 force per cell before contact was within the level of noise as expected for isolated cells and
297 increased within 30 minutes after contact to reach a plateau, attesting the capacity of all three
298 cell lines to transmit intercellular tugging forces across the junction (Fig.8b,c). However, in
299 NMIIA KD cells, the resultant forces per cell at the plateau was significantly lower than in Ctrl
300 and NMIIB KD cell doublets (Fig.8c), which is consistent with the inability of these cells to apply
301 strong traction forces on fibronectin substratum.

302 Using traction force measurement data, we then computed the intracellular stress in the cell
303 doublets⁸⁵ (Fig. 8a). The in-plane stress is represented by a tensor with three independent
304 components: two components of normal stress denoting either tension (positive values) or
305 compression (negative values) along the corresponding directions, and one component of
306 shear stress, except in the basis of the tensor's principle directions, where there is no shear
307 stress. The ellipse representation in Figure 8a shows that the stress is highly anisotropic, and

308 the cells are mostly under tension except for regions of very small compression associated to
309 high tension in the other direction. The NMIIA KD cells show lower tension, consistent with the
310 lower amount of traction forces they exert. We focused on the normal stress within the region
311 of cell-cell junction, as AJs provide a mechanical link that drives transmission of forces between
312 cells and thus organize inter-cellular stress^{85,86}. We thus computed the perpendicular (σ_{\perp}) and
313 parallel (σ_{\parallel}) components of normal stress relative to the junction axis, which characterise the
314 tension across and along the junction respectively. Within 30 minutes after contact formation,
315 the junction was submitted to a rise of σ_{\perp} in all three cell lines, consistently with the emergence
316 of a cell-cell tugging force (Supplementary Fig.5d,e). However, in Ctrl cells, the normal stress
317 parallel to the junction σ_{\parallel} , remained higher than σ_{\perp} on average (Fig.8d). Strikingly, this was not
318 the case in NMIIIB KD and NMIIA KD cells that exhibited on average equal amounts of normal
319 stress parallel and perpendicular to the junction, denoting a more isotropic distribution of
320 junctional tension (Fig. 8d).

321 Altogether, these results show that NMIIA and NMIIIB are both required for mechanical integrity
322 of the junction. NMIIA is necessary for generation of a high junctional inter-cellular stress
323 through production of tugging forces compensated by traction applied at cell-matrix adhesions.
324 NMIIIB, on the other hand, is necessary for the establishment of an anisotropic stress at the
325 junction, sustaining high tension along the cell-cell interface.

326

327 **Discussion**

328 Here, we explore for the first time the involvement of NMII isoforms during early steps of
329 epithelial junction formation. We show that NMIIA and NMIIIB associate with distinct pools of
330 actin and cooperate to initiate the formation of epithelial AJ before the acquisition of the apico-
331 basal polarization (See model, Supplementary Fig.6).

332 While NMIIA associated to actin bundles parallel to- and distant from the junction, NMIIIB was
333 sitting at junctional membranes in association with an Arp2/3-branched actin network, distinct
334 from NMIIA-associated actin. The existence of two distinct actin networks at *adherens*
335 junctions had already been observed in early junctions between hepatocytes¹⁸ and in

336 endothelial cells where VE-cadherin was shown to colocalize with Arp2/3 complex-positive
337 actin networks in-between distal actin-NMII bundles⁶⁵. The localization of NMIIA is reminiscent
338 of what has been observed previously in linear AJ of endothelial cells⁶⁵. Strikingly, we show
339 here an unexpected association of NMIIIB with the Arp2/3-dependant branched actin that link
340 the junctional membrane to NMIIA-associated perijunctional contractile actin bundles. Our data
341 support a role of this isoform in organizing this branched network and its association to
342 adhesion complexes on one side and perijunctional actin bundle on the other side. We believe
343 that these are properties common to the early stage of AJ formation in many cell types^{18,65}, that
344 then mature to elaborate *zonulae adherens* in epithelial cells where both actin organizations,
345 associated with their respective NMII isoforms, persist but become tightly packed to the
346 junctional membrane^{14,32}. Interestingly, in the absence of α -catenin KD, the localization of
347 NMIIIB was not restricted any more to junctional membranes in early epithelial junctions.
348 Instead, NMIIIB co-assembled with NMIIA on the same actin fibres, likely in heterotypic
349 minifilaments, as observed in previous studies^{36,61}, indicating that α -catenin is responsible for
350 the junctional recruitment of NMIIIB, as reinforced by a recent publication reporting NMIIIB and
351 α -catenin interaction in glioblastoma cells⁷³.

352 These distinct localization patterns at early junctions are correlated to differential contributions
353 of NMIIA and NMIIIB in junction biogenesis. Upon contact formation, NMIIA KD cells were
354 unable to elongate the junction and to sustain long-lived cell-cell contacts. They also lacked
355 the capacity to produce traction forces on E-cadherin-coated substrates. Our observations thus
356 identify NMIIA as the major isoform responsible for the NMII-dependent mechanical tugging
357 force required for junction growth²⁹. This was confirmed by traction force and stress analysis
358 data revealing a decrease of the forces as well as a reduction of both parallel and perpendicular
359 stresses at the junction for NMIIA KD cells. In contrast, NMIIIB KD cells transmitted elevated
360 tugging forces and maintained cell-cell contacts, but their junctions appeared enlarged and
361 twisted with a lower parallel stress. These results are remarkable given that NMIIIB was found
362 to be expressed 100 times less than NMIIA in MDCK cells³⁵. NMIIIB was required for efficient

363 E-cadherin clustering on E-cadherin substrates and for the connection of the contractile actin
364 network to these clusters. NMIIB was also required for the proper organization and spatial
365 restriction of the Arp2/3-dependent branched actin in the junctional area. Unexpectedly, NMIIB,
366 and not NMIIA, was the main isoform responsible for the maintenance of α -catenin in an
367 opened conformation.

368 Given that E-cadherin complexes have been shown to biochemically interact with both
369 Arp2/3^{16,77} and NMIIB⁷³, one hypothesis could be that NMIIB and Arp2/3 are both recruited to
370 E-cadherin/catenin complexes upon cell-cell contact initiation. NMIIB could thus serve as a
371 cross-linker of the junctional actin network. Hence, the absence of NMIIB may induce a local
372 softening of AJs which in turn leads to reduced extension of AJs and keeps α -catenin in a
373 closed conformation. It is also in agreement with a previous study showing that Arp2/3-
374 nucleated actin network at the *zonula adherens* regulates junctional tension and integrity⁷⁷.
375 NMIIB by associating both with cadherin-catenin complexes and the branched actin could
376 somehow rigidify and regulate the thickness of this F-actin cushion sitting between the
377 membrane and the contractile actin fibres associated to NMIIA. This could be achieved through
378 the specific biochemical properties of NMIIB towards actin that provide it with the capacity to
379 transmit tension within actin filaments at low energetic cost^{39,87,88}. Along this line, it is striking
380 to note that we never observe in early AJ any sign of organization of NMIIB in minifilaments in
381 the junctional area as observed for NMIIA in perijunctional actin bundles.

382 Inter-cellular stress is generated at cell-cell adhesions, although this remained poorly
383 characterized^{80,81}. Here, we evaluated the amount and the orientation of intercellular stress
384 generated during junction biogenesis. Within one hour of cell-cell contact, an anisotropic inter-
385 cellular stress appeared at the junction, with a preferential orientation parallel to the junction,
386 favouring the elongation and the stability of the nascent junction. Both isoforms were required
387 for proper establishment and orientation of this inter-cellular stress. NMIIA silencing had a
388 global impact on the amount of inter-cellular stress generated, which was not surprising given
389 its role on traction force production both at cell-matrix and cell-cell adhesions. On the other
390 hand, NMIIB favoured the production of a higher parallel inter-cellular stress, probably by

391 driving the crosslinking and stiffening of the junctional actin network that couples the
392 perijunctional contractile actin to the plasma membrane.

393 In conclusion, we demonstrate here that both NMIIA and NMIIB contribute to the early steps
394 of AJ biogenesis and are necessary for mechanical integrity of the junction, albeit implicated
395 in very different aspects of adhesion complexes and actin pools organization. These findings
396 open new avenues in the understanding of how distinct pools of actomyosin, associated to
397 different myosin isoforms, built up and integrate mechanical forces to regulate adherens
398 junction remodelling and intercellular stress in vertebrate cells in order to achieve large scale
399 tissue remodelling during embryogenesis and tissue repair.

400

401 **Methods**

402 **Antibodies and reagents**

403 The following primary antibodies were used: rabbit anti-NMIIA polyclonal (Biolegend) or
404 mouse anti-NMIIA monoclonal antibodies (Abcam, for co-immunostainings with anti-NMIIB
405 antibodies); rabbit anti- β -catenin polyclonal (Sigma-Aldrich) or mouse anti- β -catenin
406 monoclonal (BD Biosciences) antibodies; recombinant rabbit anti-paxillin monoclonal
407 antibody (Abcam); mouse anti-GAPDH (ProteinTech), mouse anti-Arp3 (Sigma-Aldrich) and
408 mouse anti-E-cadherin (BD Biosciences) antibodies; rabbit anti- α -catenin polyclonal (Sigma-
409 Aldrich) and rabbit anti-NMIIB polyclonal (Biolegend) antibodies; rat anti- α 18-catenin
410 monoclonal antibody (generously provided by A. Nagafuchi (Kumamoto University, Japan)⁸⁹.
411 Alexa488-, Alexa568- and Alexa647-conjugated secondary antibodies were purchased from
412 ThermoFisher, Alexa (488 or 555 or 647) -coupled phalloidins from Invitrogen and Hoechst
413 34580 from ThermoFisher. Horseradish peroxidase-coupled anti-mouse IgGs (Sigma-
414 Aldrich) and anti-rabbit IgGs (Pierce) were used for immunoblotting. Mitomycin C and Y-
415 27632 dihydrochloride were purchased from Sigma-Aldrich. The APP (Azido-Poly-lysine Poly
416 (ethylene glycol)) and the BCN-RGD peptide (BCN: bicyclo[6.1.0]- nonyne, coupled to RGD:
417 peptide sequence Arg-Gly-Asp) were prepared as previously described⁹⁰.

418 **Cell culture**

419 MDCK (ATCC CCL-34) and C2C12 (ATCC CRL-1772) cells originate from the American
420 Type Culture Collection (ATCC). E-cadherin-GFP⁹¹ and α -catenin KD MDCK cell lines⁹² were
421 kindly provided by W.J. Nelson (Stanford University, Palo Alto). Caco2BBE cells (ATCC
422 HTB-37) were kindly provided by S. Robine (Institut Curie/CNRS, Paris). Cells were
423 maintained at 37°C, 5% CO₂ in DMEM (containing Glutamax, High Glucose and Pyruvate,
424 Life Technologies) supplemented with 100 μ g/mL Penicillin/Streptomycin (Life Technologies)
425 and Foetal Bovine Serum (Life Technologies) at 10% for MDCK and C2C12 cells and at 20%
426 for Caco2 cells. Ecadherin-GFP cells and α -catenin KD MDCK cells were maintained in
427 media containing 5 μ g/ml geneticin (Life Technologies).

428

429 **Generation of isoform-specific NMII knock-down MDCK cell lines**

430 For generation of isoform-specific NMII Heavy chain knock-down cells, isoform-specific
431 shRNA sequences, inserted in a back bone standard vector pLKO.1-puro, were designed
432 and synthesized by Sigma-Aldrich technical services, based on the sequences of *Canis lupus*
433 *familiaris* transcripts for MYH9 (NMIIA, transcript ID: ENSCAFT00000002643.3) and MYH10
434 (NMIIB, transcript ID: ENSCAFT000000027478). The sequences used were the following:
435 TTGGAGCCATACAACAATAC for NMIIA and TCGGGCAGCTCTACAAAGAAT for NMIIB.
436 As a control, the pLKO.1-puro non-mammalian shRNA Control Plasmid DNA was used
437 (SHC002, Sigma-Aldrich). Two million Ecadherin-GFP MDCK cells were electroporated
438 (Neon Transfection System Invitrogen) with 3-5 μ g shRNA encoding plasmids in one pulse of
439 20 ms at 1650 V. Twenty four hours later, cells were put under selection pressure by adding
440 puromycin (2.5 μ g/ml) in media. After 10 days, single cells were sorted in 96 well plates by
441 flow cytometry using Influx 500 sorter-analyzer (BD BioSciences) and clonal populations then
442 selected based on NMII isoform expression levels by immunoblot and immunofluorescence.

443 Control, NMIIA KD and NMIIB KD MDCK cells were maintained in media containing geneticin
444 (5 µg/ml) and puromycin (2.5 µg/ml).

445 For simultaneous visualization of E-cadherin and centrosome, Ecadherin-GFP MDCK cells
446 were transiently transfected with a plasmid driving the expression of RFP-Pericentrin (kindly
447 provided M. Coppey, Institut Jacques Monod, Paris), using the protocol described above,
448 one or two days before the experiment. m-Cherry cortactin plasmids (kindly provided by
449 Alexis Gautreau, Biochemistry laboratory, Ecole polytechnique, France) were transfected in
450 Control, NMIIA KD and NMIIB KD MDCK cells and the m-cherry expressing cell population
451 was sorted by flow cytometry using Influx 500 sorter-analyzer (BD BioSciences).

452

453 **Western blotting**

454 Confluent cells were lysed in 100 mM Tris pH 7.5, 150 mM NaCl, 0.5% NP40, 0.5% Triton-
455 X100, 10% glycerol, 1X protease inhibitor cocktail (Roche) and 1X phosphatase inhibitor
456 (Phosphostop, Roche) for 20 minutes at 4°C. Insoluble debris were centrifuged for 15
457 minutes at 13000 g and supernatants were recovered. Protein concentration was quantified
458 by Bradford assay (BioRad), SDS PAGE and electrotransfer were performed on 4-12% Bis-
459 Tris gel (Novex) using mini gel tank and iBlot transfer systems (Invitrogen). Non-specific sites
460 were blocked with 5% non-fat dry milk in PBS 0.1% Tween 20. Primary antibodies were
461 diluted (1/1000) in PBS 0.1% Tween 20 and incubated overnight at 4°C. After three washes
462 in PBS 0.1% Tween 20, secondary HRP antibodies diluted in PBS 0.1% Tween 20 (1/10000)
463 were incubated for 1 hour and washed 3 times with PBS 0.1% Tween 20. Immunocomplexes
464 of interest were detected using Supersignal West Femto Maximum Sensitivity Substrate
465 (ThermoFisher) and visualized with ChemiDoc chemoluminescence detection system
466 (Biorad). Quantification of Western blots by densitometry was performed using the Gel
467 analyzer plug in from Image J. GAPDH was used as a loading control to normalize the
468 quantification.

469 **Immunofluorescent staining**

470 Cells were fixed with pre-warmed 4% formaldehyde in PBS for 15 min at RT and then
471 washed 3 times with PBS, followed by permeabilization and blocking with 0.05%
472 saponin/0.2% BSA in PBS for 15 minutes at RT. The primary antibodies diluted (1/100) in
473 Saponin/BSA buffer were then incubated overnight at 4°C. After 3 washes in Saponin/BSA
474 buffer, the samples were incubated with secondary antibodies and, when indicated, Alexa-
475 coupled phalloidin, diluted at 1/200 in the same buffer for 1 hour at RT. The preparations
476 were washed twice in Saponin/BSA buffer, once in PBS, and then mounted with the DAPI
477 Fluoromount-G mounting media (Southern Biotech).

478

479 **Preparation of fibronectin-coated and cadherin-coated substrates**

480 For fibronectin coating, glass coverslips were first cleaned by sonication in 70% ethanol and
481 air dried. They were coated for 1 hour with 50 µg/mL human plasma fibronectin (Merck
482 Millipore) diluted in PBS and washed three times with PBS.

483 The protocol for E-cadherin coating was inspired from a previous study by Lee and
484 colleagues⁹³. Briefly, the cleaned glass coverslips were silanized with 10% 3-aminopropyl
485 triethoxysilane (APTES, Sigma-Aldrich) in 100% ethanol for 10 minutes at RT, washed once
486 in 100% ethanol and dried at 80°C for 10 minutes. The surface was then functionalized by
487 incubation for 1 hour with 2 mM EDC-HCl (Thermo Scientific) / 5 mM NHS (Sigma-Aldrich)
488 and 1 µg of recombinant human E-cadherin (R&D systems). Coverslips were then washed
489 two times with PBS.

490 Cells were plated at very low density (typically 1 10⁵ cells for a 32 mm diameter coverslip) on
491 the coated coverslips in complete medium containing 10 µg/mL mitomycin C. After 1 hour
492 incubation at 37°C, the preparations were washed twice with complete media and incubated
493 2-6 hours or overnight at 37°C before imaging or fixation, for cadherin coating and fibronectin
494 coating, respectively.

495 **Preparation of switchable micro-patterns and imaging**

496 Micropatterns were made as previously described with some modifications⁹⁴. Briefly, air dried
497 cleaned glass coverslips were activated with deep UV for 5 minutes, and coated for at least 1
498 hour with the repellent compound APP (0.1mg/ml in HEPES 10 mM pH7.4). After 3 washes
499 with deionized water, the coverslips were exposed to deep UV for 7 minutes through a
500 chrome photomask. The coverslips were then washed with deionized water three times,
501 coated with 50 µg/mL human plasma fibronectin for 1 hour and washed twice with deionized
502 water and once with PBS. When indicated, the coating was done with a 2:1 ratio of non-
503 coupled: Cy3-coupled fibronectin prepared with Cy3 Mono-Reactive Dye Pack (GE
504 Healthcare) as recommended by the manufacturer.

505 Cells were resuspended at $4 \cdot 10^2$ cells/mm² in medium containing 10 µg/mL mitomycin C and
506 deposited on the patterned slide. After 1 hour of incubation at 37°C, cells were washed 3
507 times with fresh medium to remove mitomycin C and cells that remained in suspension. The
508 cells that adhered on micro-patterns were left overnight in the incubator. The day after,
509 confinement was released by addition of 20 µM BCN-RGD peptide diluted in DMEM media
510 or, in case of live-imaging experiments, in Fluorobrite DMEM (Thermo Fisher) supplemented
511 with 10% FBS and 1% Penicillin/Streptomycin. For ROCK inhibition experiments, 50 µM Y-
512 27632 was added at the same time as BCN-RGD. Samples were then immediately imaged
513 under a microscope or left in the incubator for 20 more hours and fixed as described above.
514 When indicated for live-imaging experiments, nuclei were stained before adding BCN-RGD
515 peptide by incubating the preparations with 5 µg/mL Hoechst 34580 in the medium for 20
516 minutes at 37°C followed by two washes with fresh media.

517

518 **Image acquisition and analysis**

519 For live-microscopy experiments, the samples were placed in a chamber equilibrated at 37°C
520 under 5% CO₂ atmosphere. Images were acquired with a Yokogawa-Andor CSU-W1

521 Spinning Disk confocal mounted on an inversed motorised Leica DMI8 microscope and
522 equipped with a sCMOS Orca-Flash 4 V2+ camera (Hamamatsu) and a 63 X oil immersion
523 objective or a 20 X dry objective, with multi-positioning and a resolution of 0.5-3 μm z-stacks.
524 Alternatively, the samples were imaged with an Olympus IX81 wide-field fluorescence
525 microscope equipped with a Coolsnap HQ CCD camera and a 60X oil immersion objective or
526 a 20 X dry objective. For some experiments, the Nikon Biostation IM-Q microscope was also
527 used with 10X or 20X objective and multi-positioning.

528 For fixed samples, images were acquired with a Zeiss Apotome fluorescence microscope
529 equipped with a 63 X oil immersion objective or with a Zeiss LSM 780 confocal microscope
530 equipped with a 63 X oil immersion objective at a resolution of 0.3 μm z-stacks.

531 Image processing and analysis were done on Fiji software. Analysis of junction parameters
532 (length, straightness and angle deviation) was done manually with Fiji software based on
533 phase contrast and GFP-Ecadherin signal. Cell spreading, focal adhesions and α -catenin
534 clustering were analyzed by thresholding the image and applying an “Analyze particles”
535 which gives the number of objects and its area. To calculate the ratio of α -cat to α 18-cat
536 intensities, the mean grey intensity value for the two channels were measured within the
537 manually-defined junction. Tracking of single cells on fibronectin was done using the Manual
538 Tracking plugin.

539

540 **Traction force microscopy**

541 Soft silicone elastomer substrates for TFM (Traction force microscopy) were prepared as
542 described previously with some modifications⁹⁵. Cy 52-276 A and Cy 52-276 B silicone
543 elastomer components (Dow corning) were mixed in a 5:5 (elastic modulus \sim 15 kPa for E-
544 cadherin-coating) or a 5:6 ratio (elastic modulus \sim 30 kPa for fibronectin-coating). 0.08 g of
545 elastomer was deposited on 32 mm glass coverslips and allowed to spread progressively.
546 The substrate was silanized with 10 % (3-aminopropyl triethoxysilane (APTES, Sigma) in

547 100% ethanol for 10 minutes at RT, washed once in 100 % ethanol and dried at 80°C for 10
548 minutes. The surface was coated for 10 minutes at RT with carboxylated red fluorescent
549 beads (100 nm, Invitrogen) diluted at 2-3/1000 in deionized water. After washing with
550 deionized water, the surface was finally functionalized with protein (fibronectin or E-cadherin)
551 as described above. Seeded cells together with fluorescent beads were imaged either on an
552 Olympus-CSU-W1 Spinning Disk confocal microscope with a 10 X dry objective and 3 μm z
553 stacks or on an Olympus-IX81 wide field inverted fluorescence microscope with a 20 X dry
554 objective for 2 to 24 hours, at a frequency of 1 frame every 10 min, at 37°C under 5% CO₂
555 atmosphere. At the end of the acquisition, 100-200 μL of 10% SDS was added in the media
556 to detach cells and image a reference frame. For force calculation, matPIV was used to
557 analyse the displacement vectors of the beads, which were further translated into forces
558 using the FTTC plugin in ImageJ. The vector quiver plots and heat map of magnitude force
559 was plotted using Matlab. Mean (resp. resultant) forces exerted by cells and doublets were
560 obtained by computing the average of the magnitude (resp. the vectorial sum) of traction
561 forces within manually defined masks. For the analysis of tractions forces below cell-cell
562 junctions, the junction masks and corresponding midline were first manually defined based
563 on the E-cadherin-GFP pictures. Then, the midline was used to define the average
564 orientation of the junction, and all force vectors within the junction mask were projected onto
565 the directions parallel and perpendicular to this orientation. The mask was divided in four
566 quarters along this mean orientation. The “junction centre parallel (resp. perpendicular) force”
567 is defined as the averaged absolute value of the parallel (resp. perpendicular) component of
568 traction forces in the two central quarters of the mask, while the “junction periphery parallel
569 (resp. perpendicular) force” is the averaged absolute value of the parallel (resp.
570 perpendicular) component of traction forces in the two outermost quarters.

571 $T_{(\text{parallel} / \text{perpendicular})}^{(\text{center/periphery})} = \langle |T_{(\text{parallel} / \text{perpendicular})}| \rangle_{(\text{center} /$
572 $\text{periphery})}$

573

574 **Calculation of inter-cellular stress**

575 Computing the junctional stress components σ_{\parallel} and σ_{\perp} , respectively parallel and
576 perpendicular to the cell junction (Fig. 8d), required both the determination of the cell junction
577 location and the estimation of the inter-cellular stress tensor. The cell junction domain was
578 defined as the overlap between two masks representing the area covered by each cell in the
579 doublet. Given the stress tensor, the parallel and perpendicular stress components were
580 obtained by rotation from the cartesian basis. As exemplified in Fig. 8a, we found in most
581 cases that the cell junction domain was roughly straight: the mean orientation of the cell
582 junction domain determined the rotation angle. We checked that following the cell junction
583 contour did not significantly modify our estimates. Finally, each junctional stress component
584 was spatially-averaged over the cell junction domain.

585 Intercellular stress was estimated by Bayesian inversion⁹⁶, with a dimensionless
586 regularization parameter $\Lambda = 10^5$ (see ⁸ for details). The spatial domain for stress estimation
587 was for each image the smallest rectangle encompassing the cell doublet. For simplicity, we
588 implemented free stress boundary conditions on the straight boundaries of the rectangular
589 domain, instead of following the cell doublet boundaries. As a consequence, the stress
590 estimation was qualitative, but sufficed to evaluate differences between conditions. Note that
591 height variations within the cell doublet were also neglected in the estimation of the 2D inter-
592 cellular stress field.

593

594 **SIM microscopy**

595 Super-resolution structured-illumination microscopy was performed on a Zeiss Elyra PS.1
596 microscope with a 63 X objective (Plan Apo 1.4NA oil immersion) and an additional optovar
597 lens 1.6 X. Cells grown on 0.17 mm high-performance Zeiss coverslips were fixed and
598 prepared for immunostaining, then with DAPI Fluoromount-G mounting media (Southern
599 Biotech). Laser lines 488 nm, 561 nm and 641 nm were directed into the microscope,

600 passing through a diffraction grating. For 3D SIM imaging, the diffraction grating was rotated
601 along 3 directions (angles 120°) and translated (five lateral positions) throughout the
602 acquisition. Typically, 20-30 slices of 110 nm were acquired for each cell corresponding to an
603 imaging height of 2-3 µm. The fluorescence signal was detected with an EMCCD camera
604 (iXon-885, Andor, 1004x1002, pixel size 8 µm, QE=65%). Processed SIM images were
605 aligned via an affine transformation matrix of predefined values obtained using 100 nm
606 multicolor Tetraspeck fluorescent microspheres (Thermo Fisher Scientific).

607

608 **Data display and statistics**

609 Images were mounted using Photoshop and Illustrator. Graphs and statistical tests were
610 done using GraphPad prism software.

611

612 **Acknowledgements**

613 This work was supported by the European Research Council (Grant No. CoG-617233), LABEX
614 “Who Am I?,” and the Agence Nationale de la Recherche “POLCAM” (Grant No. ANR-17-
615 CE13-0013). We acknowledge the ImagoSeine core facility of the Institut Jacques Monod,
616 member of IBISA and France-BioImaging (ANR-10-INBS-04) infrastructures. We thank Orestis
617 (ImagoSeine core facility, IJM) for technical assistance with SIM experiments. We thank Sree
618 Vaishnavi and Gianluca Greci (Micro fabrication Core Facility of Mechnabiology Institute,
619 National University of Singapore) for the fabrication of chrome photomask. We thank A.
620 Nagafuchi for α 18-catenin antibody, W.J. Nelson and S. Robine for providing cells, M. Coppey
621 for RFP-Pericentrin plasmid and M. Piel (IPGG, Curie Institute) for providing original APP and
622 BCN-RGD compounds. We thank Delphine Delacour and Shreyansh Jain for useful scientific
623 discussions and critical reading of the manuscript.

624

625

626 **Author contributions**

627 R.M.M, B.L. and M.H.L. conceived the project. R.M.M and B.L. supervised the project. M.L.H,
628 G.S and T.D performed experiments. M.L.H, G.S., R.M.M and B.L. designed experiments and
629 analyzed data. J.A., V.C and P.M analyzed traction force microscopy data and calculated inter-
630 cellular stress. D.W and J.v.H designed and performed the production of APP and BCN-RGD
631 compounds. M.L.H, G.S., R.M.M, B.L. J.A., V.C and P.M wrote the manuscript.

632

633 **Competing Interests statement**

634 The authors declare no competing interests.

635

636

637 **References**

638

- 639 1. Adams, C. L., Chen, Y. T., Smith, S. J. & Nelson, W. J. Mechanisms of epithelial cell-
640 cell adhesion and cell compaction revealed by high-resolution tracking of E-cadherin-
641 green fluorescent protein. *J. Cell Biol.* **142**, 1105–1119 (1998).
- 642 2. Green, K. J., Getsios, S., Troyanovsky, S. & Godsel, L. M. Intercellular junction
643 assembly, dynamics, and homeostasis. *Cold Spring Harbor perspectives in biology* **2**,
644 a000125 (2010).
- 645 3. Takeichi, M. Dynamic contacts: rearranging adherens junctions to drive epithelial
646 remodelling. *Nat. Rev. Mol. Cell Biol.* **15**, 397–410 (2014).
- 647 4. Mège, R. M. & Ishiyama, N. Integration of Cadherin Adhesion and Cytoskeleton at
648 *Adherens Junctions*. *Cold Spring Harb. Perspect. Biol.* **9**, a028738 (2017).
- 649 5. Cavey, M., Rauzi, M., Lenne, P.-F. & Lecuit, T. A two-tiered mechanism for
650 stabilization and immobilization of E-cadherin. *Nature* **453**, 751–6 (2008).
- 651 6. Maître, J.-L., Niwayama, R., Turlier, H., Nédélec, F. & Hiiragi, T. Pulsatile cell-
652 autonomous contractility drives compaction in the mouse embryo. *Nat. Cell Biol.* **17**,
653 849–855 (2015).

- 654 7. Jacinto, A. *et al.* Dynamic analysis of actin cable function during *Drosophila* dorsal
655 closure. *Curr. Biol.* **12**, 1245–50 (2002).
- 656 8. Harris, A. R., Daeden, A. & Charras, G. T. Formation of adherens junctions leads to
657 the emergence of a tissue-level tension in epithelial monolayers. *J. Cell Sci.* **127**,
658 2507–17 (2014).
- 659 9. Kocgozlu, L. *et al.* Epithelial Cell Packing Induces Distinct Modes of Cell Extrusions.
660 *Curr. Biol.* **26**, 2942–2950 (2016).
- 661 10. Wood, W. *et al.* Wound healing recapitulates morphogenesis in *Drosophila* embryos.
662 *Nat. Cell Biol.* **4**, 907–912 (2002).
- 663 11. Yap, A. S., Briehner, W. M., Pruschy, M. & Gumbiner, B. M. Lateral clustering of the
664 adhesive ectodomain: A fundamental determinant of cadherin function. *Curr. Biol.* **7**,
665 308–315 (1997).
- 666 12. Strale, P. O. *et al.* The formation of ordered nanoclusters controls cadherin anchoring
667 to actin and cell-cell contact fluidity. *J. Cell Biol.* **210**, 333–346 (2015).
- 668 13. Adams, C. L., Chen, Y. T., Smith, S. J. & Nelson, W. J. Mechanisms of epithelial cell-
669 cell adhesion and cell compaction revealed by high-resolution tracking of E-cadherin-
670 green fluorescent protein. *J. Cell Biol.* **142**, 1105–19 (1998).
- 671 14. Mège, R. M., Gavard, J. & Lambert, M. Regulation of cell-cell junctions by the
672 cytoskeleton. *Current Opinion in Cell Biology* **18**, 541–548 (2006).
- 673 15. Grikscheit, K., Frank, T., Wang, Y. & Grosse, R. Junctional actin assembly is mediated
674 by Formin-like 2 downstream of Rac1. *J. Cell Biol.* **209**, 367–376 (2015).
- 675 16. Kovacs, E. M., Goodwin, M., Ali, R. G., Paterson, A. D. & Yap, A. S. Cadherin-directed
676 actin assembly: E-cadherin physically associates with the Arp2/3 complex to direct
677 actin assembly in nascent adhesive contacts. *Curr. Biol.* **12**, 379–382 (2002).
- 678 17. Yamada, S. & Nelson, W. J. Localized zones of Rho and Rac activities drive initiation
679 and expansion of epithelial cell-cell adhesion. *J. Cell Biol.* **178**, 517–527 (2007).
- 680 18. Krendel, M. F. & Bonder, E. M. Analysis of actin filament bundle dynamics during
681 contact formation in live epithelial cells. *Cell Motil. Cytoskeleton* **43**, 296–309 (1999).

- 682 19. Chu, Y. S. *et al.* Force measurements in E-cadherin-mediated cell doublets reveal
683 rapid adhesion strengthened by actin cytoskeleton remodeling through Rac and
684 Cdc42. *J. Cell Biol.* **167**, 1183–1194 (2004).
- 685 20. Borghi, N. *et al.* E-cadherin is under constitutive actomyosin-generated tension that is
686 increased at cell-cell contacts upon externally applied stretch. *Proc. Natl. Acad. Sci.*
687 **109**, 12568–12573 (2012).
- 688 21. Curran, S. *et al.* Myosin II Controls Junction Fluctuations to Guide Epithelial Tissue
689 Ordering. *Dev. Cell* (2017). doi:10.1016/j.devcel.2017.09.018
- 690 22. Ladoux, B. & Mège, R.-M. Mechanobiology of collective cell behaviours. *Nat. Rev.*
691 *Mol. Cell Biol.* nrm.2017.98 (2017). doi:10.1038/nrm.2017.98
- 692 23. Salomon, J. *et al.* Contractile forces at tricellular contacts modulate epithelial
693 organization and monolayer integrity. *Nat. Commun.* **8**, 13998 (2017).
- 694 24. Munjal, A. & Lecuit, T. Actomyosin networks and tissue morphogenesis. *Development*
695 **141**, 1789–1793 (2014).
- 696 25. Tamada, M., Perez, T. D., Nelson, W. J. & Sheetz, M. P. Two distinct modes of
697 myosin assembly and dynamics during epithelial wound closure. *J. Cell Biol.* **176**, 27–
698 33 (2007).
- 699 26. Begnaud, S., Chen, T., Delacour, D., Mège, R. M. & Ladoux, B. Mechanics of
700 epithelial tissues during gap closure. *Current Opinion in Cell Biology* **42**, 52–62 (2016).
- 701 27. Rosenblatt, J., Raff, M. C. & Cramer, L. P. An epithelial cell destined for apoptosis
702 signals its neighbors to extrude it by an actin- and myosin-dependent mechanism.
703 *Curr. Biol.* **11**, 1847–1857 (2001).
- 704 28. Weng, M. & Wieschaus, E. Myosin-dependent remodeling of adherens junctions
705 protects junctions from Snail-dependent disassembly. *J. Cell Biol.* **212**, 219–29 (2016).
- 706 29. Liu, Z. *et al.* Mechanical tugging force regulates the size of cell-cell junctions. *Proc.*
707 *Natl. Acad. Sci.* **107**, 9944–9949 (2010).
- 708 30. Hoelzle, M. K. & Svitkina, T. The cytoskeletal mechanisms of cell-cell junction
709 formation in endothelial cells. *Mol. Biol. Cell* **23**, 310–323 (2012).

- 710 31. Shewan, A. M. *et al.* Myosin 2 is a key Rho kinase target necessary for the local
711 concentration of E-cadherin at cell-cell contacts. *Mol. Biol. Cell* **16**, 4531–42 (2005).
- 712 32. Smutny, M. *et al.* Myosin II isoforms identify distinct functional modules that support
713 integrity of the epithelial zonula adherens. *Nat. Cell Biol.* **12**, 696–702 (2010).
- 714 33. Vicente-Manzanares, M., Ma, X., Adelstein, R. S. & Horwitz, A. R. Non-muscle myosin
715 II takes centre stage in cell adhesion and migration. *Nat. Rev. Mol. Cell Biol.* **10**, 778–
716 790 (2009).
- 717 34. Conti, M. A. & Adelstein, R. S. Nonmuscle myosin II moves in new directions. *J. Cell*
718 *Sci.* **121**, 11–8 (2008).
- 719 35. Ma, X. *et al.* Ablation of Nonmuscle Myosin II-B and II-C Reveals a Role for
720 Nonmuscle Myosin II in Cardiac Myocyte Karyokinesis. *Mol. Biol. Cell* **21**, 3952–3962
721 (2010).
- 722 36. Beach, J. R. & Hammer, J. A. Myosin II isoform co-assembly and differential regulation
723 in mammalian systems. *Experimental Cell Research* **334**, 2–9 (2015).
- 724 37. Wang, F. *et al.* Kinetic mechanism of non-muscle myosin IIB. Functional adaptations
725 for tension generation and maintenance. *J. Biol. Chem.* **278**, 27439–27448 (2003).
- 726 38. Kovács, M., Wang, F., Hu, A., Zhang, Y. & Sellers, J. R. Functional divergence of
727 human cytoplasmic myosin II. Kinetic characterization of the non-muscle IIA isoform.
728 *J. Biol. Chem.* **278**, 38132–38140 (2003).
- 729 39. Kovács, M., Thirumurugan, K., Knight, P. J. & Sellers, J. R. Load-dependent
730 mechanism of nonmuscle myosin 2. *Proc. Natl. Acad. Sci. U. S. A.* **104**, 9994–9
731 (2007).
- 732 40. Billington, N., Wang, A., Mao, J., Adelstein, R. S. & Sellers, J. R. Characterization of
733 three full-length human nonmuscle myosin II paralogs. *J. Biol. Chem.* **288**, 33398–
734 33410 (2013).
- 735 41. Sandquist, J. C. & Means, A. R. The C-Terminal Tail Region of Nonmuscle Myosin II
736 Directs Isoform-specific Distribution in Migrating Cells. *Mol. Biol. Cell* **19**, 5156–5167
737 (2008).

- 738 42. Juanes-Garcia, A. *et al.* A regulatory motif in nonmuscle myosin II-B regulates its role
739 in migratory front-back polarity. *J. Cell Biol.* **209**, 23–32 (2015).
- 740 43. Chang, C.-W. & Kumar, S. Differential Contributions of Nonmuscle Myosin II Isoforms
741 and Functional Domains to Stress Fiber Mechanics. *Sci. Rep.* **5**, 13736 (2015).
- 742 44. Shutova, M. S., Spessott, W. A., Giraudo, C. G. & Svitkina, T. Endogenous species of
743 mammalian nonmuscle myosin IIA and IIB include activated monomers and
744 heteropolymers. *Curr. Biol.* **24**, 1958–1968 (2014).
- 745 45. Beach, J. R. *et al.* Nonmuscle myosin II isoforms coassemble in living cells. *Curr. Biol.*
746 **24**, 1160–1166 (2014).
- 747 46. Skoglund, P., Rolo, A., Chen, X., Gumbiner, B. M. & Keller, R. Convergence and
748 extension at gastrulation require a myosin IIB-dependent cortical actin network.
749 *Development* **135**, 2435–2444 (2008).
- 750 47. Wang, A., Ma, X., Conti, M. A. & Adelstein, R. S. Distinct and redundant roles of the
751 non-muscle myosin II isoforms and functional domains. *Biochem. Soc. Trans.* **39**,
752 1131–5 (2011).
- 753 48. Haque, F. *et al.* Non-muscle myosin II deletion in the developing kidney causes ureter-
754 bladder misconnection and apical extrusion of the nephric duct lineage epithelia. *Dev.*
755 *Biol.* **427**, 121–130 (2017).
- 756 49. Ridge, L. A. *et al.* Non-muscle myosin IIB (Myh10) is required for epicardial function
757 and coronary vessel formation during mammalian development. *PLOS Genet.* **13**,
758 e1007068 (2017).
- 759 50. Conti, M. A., Even-Ram, S., Liu, C., Yamada, K. M. & Adelstein, R. S. Defects in cell
760 adhesion and the visceral endoderm following ablation of nonmuscle myosin heavy
761 chain II-A in mice. *J. Biol. Chem.* **279**, 41263–41266 (2004).
- 762 51. Tullio, A. N. *et al.* Nonmuscle myosin II-B is required for normal development of the
763 mouse heart. *Proc. Natl. Acad. Sci.* **94**, 12407–12412 (1997).
- 764 52. Doyle, A. D. *et al.* Micro-environmental control of cell migration--myosin IIA is required
765 for efficient migration in fibrillar environments through control of cell adhesion

- 766 dynamics. *J. Cell Sci.* **125**, 2244–56 (2012).
- 767 53. Betapudi, V., Licate, L. S. & Egelhoff, T. T. Distinct roles of nonmuscle myosin II
768 isoforms in the regulation of MDA-MB-231 breast cancer cell spreading and migration.
769 *Cancer Res.* **66**, 4725–4733 (2006).
- 770 54. Cai, Y. *et al.* Nonmuscle Myosin IIA-Dependent Force Inhibits Cell Spreading and
771 Drives F-Actin Flow. *Biophys. J.* **91**, 3907–3920 (2006).
- 772 55. Jorrich, M. H., Shih, W. & Yamada, S. Myosin IIA deficient cells migrate efficiently
773 despite reduced traction forces at cell periphery. *Biol. Open* **2**, 368–372 (2013).
- 774 56. Kolega, J. Asymmetric distribution of myosin IIB in migrating endothelial cells is
775 regulated by a rho-dependent kinase and contributes to tail retraction. *Mol Biol Cell* **14**,
776 4745–4757 (2003).
- 777 57. Sandquist, J. C., Swenson, K. I., DeMali, K. A., Burridge, K. & Means, A. R. Rho
778 kinase differentially regulates phosphorylation of nonmuscle myosin II isoforms A and
779 B during cell rounding and migration. *J. Biol. Chem.* **281**, 35873–35883 (2006).
- 780 58. Vicente-Manzanares, M., Koach, M. A., Whitmore, L., Lamers, M. L. & Horwitz, A. F.
781 Segregation and activation of myosin IIB creates a rear in migrating cells. *J. Cell Biol.*
782 **183**, 543–554 (2008).
- 783 59. Vicente-Manzanares, M., Newell-Litwa, K., Bachir, A. I., Whitmore, L. A. & Horwitz, A.
784 R. Myosin IIA/IIB restrict adhesive and protrusive signaling to generate front-back
785 polarity in migrating cells. *J. Cell Biol.* **193**, 381–396 (2011).
- 786 60. Betapudi, V. Myosin II motor proteins with different functions determine the fate of
787 lamellipodia extension during cell spreading. *PLoS One* **5**, e8560 (2010).
- 788 61. Shutova, M. S. *et al.* Self-sorting of nonmuscle myosins IIA and IIB polarizes the
789 cytoskeleton and modulates cell motility. *J. Cell Biol.* **216**, 2877–2889 (2017).
- 790 62. Shih, W. & Yamada, S. Myosin IIA dependent retrograde flow drives 3D cell migration.
791 *Biophys. J.* **98**, L29–L31 (2010).
- 792 63. Thomas, D. G. *et al.* Non-muscle myosin IIB is critical for nuclear translocation during
793 3D invasion. *J. Cell Biol.* **210**, 583–594 (2015).

- 794 64. Raab, M. *et al.* Crawling from soft to stiff matrix polarizes the cytoskeleton and
795 phosphoregulates myosin-II heavy chain. *J. Cell Biol.* **199**, 669–683 (2012).
- 796 65. Efimova, N. & Svitkina, T. M. Branched actin networks push against each other at
797 adherens junctions to maintain cell-cell adhesion. *J. Cell Biol.* jcb.201708103 (2018).
798 doi:10.1083/jcb.201708103
- 799 66. Van Dongen, S. F. M., Maiuri, P., Marie, E., Tribet, C. & Piel, M. Triggering cell
800 adhesion, migration or shape change with a dynamic surface coating. *Adv. Mater.* **25**,
801 1687–1691 (2013).
- 802 67. Desai, R. A., Gao, L., Raghavan, S., Liu, W. F. & Chen, C. S. Cell polarity triggered by
803 cell-cell adhesion via E-cadherin. *J. Cell Sci.* **122**, 905–11 (2009).
- 804 68. Dupin, I., Camand, E. & Etienne-Manneville, S. Classical cadherins control nucleus
805 and centrosome position and cell polarity. *J. Cell Biol.* **185**, 779–86 (2009).
- 806 69. Rodríguez-Fraticelli, A. E., Auzan, M., Alonso, M. A., Bornens, M. & Martín-Belmonte,
807 F. Cell confinement controls centrosome positioning and lumen initiation during
808 epithelial morphogenesis. *J. Cell Biol.* **198**, 1011–23 (2012).
- 809 70. Burute, M. *et al.* Polarity Reversal by Centrosome Repositioning Primes Cell
810 Scattering during Epithelial-to-Mesenchymal Transition. *Dev. Cell* **40**, 168–184 (2017).
- 811 71. Stramer, B. & Mayor, R. Mechanisms and in vivo functions of contact inhibition of
812 locomotion. *Nat. Rev. Mol. Cell Biol.* **18**, 43–55 (2017).
- 813 72. Menko, A. S. *et al.* A central role for vimentin in regulating repair function during
814 healing of the lens epithelium. *Mol. Biol. Cell* **25**, 776–90 (2014).
- 815 73. Vassilev, V., Platek, A., Hiver, S., Enomoto, H. & Takeichi, M. Catenins Steer Cell
816 Migration via Stabilization of Front-Rear Polarity. *Dev. Cell* (2017).
817 doi:10.1016/j.devcel.2017.10.014
- 818 74. Benjamin, J. M. *et al.* AlphaE-catenin regulates actin dynamics independently of
819 cadherin-mediated cell-cell adhesion. *J. Cell Biol.* **189**, 339–352 (2010).
- 820 75. Choi, W. *et al.* Remodeling the zonula adherens in response to tension and the role of
821 afadin in this response. *J. Cell Biol.* **213**, 243–60 (2016).

- 822 76. Ebrahim, S. *et al.* NMII forms a contractile transcellular sarcomeric network to regulate
823 apical cell junctions and tissue geometry. *Curr. Biol.* **23**, 731–6 (2013).
- 824 77. Verma, S. *et al.* A WAVE2-Arp2/3 actin nucleator apparatus supports junctional
825 tension at the epithelial zonula adherens. *Mol. Biol. Cell* **23**, 4601–4610 (2012).
- 826 78. Ishiyama, N. *et al.* Force-dependent allostery of the α -catenin actin-binding domain
827 controls adherens junction dynamics and functions. *Nat. Commun.* **9**, 5121 (2018).
- 828 79. Yonemura, S., Wada, Y., Watanabe, T., Nagafuchi, A. & Shibata, M. α -Catenin as a
829 tension transducer that induces adherens junction development. *Nat. Cell Biol.* **12**,
830 533–542 (2010).
- 831 80. Maruthamuthu, V., Sabass, B., Schwarz, U. S. & Gardel, M. L. Cell-ECM traction force
832 modulates endogenous tension at cell-cell contacts. *Proc. Natl. Acad. Sci.* **108**, 4708–
833 4713 (2011).
- 834 81. Ng, M. R. osa, Besser, A., Brugge, J. S. & Danuser, G. Mapping the dynamics of force
835 transduction at cell-cell junctions of epithelial clusters. *Elife* **3**, e03282 (2014).
- 836 82. Ladoux, B., Nelson, W. J., Yan, J. & Mège, R. M. The mechanotransduction
837 machinery at work at adherens junctions. *Integr. Biol.* **7**, 1109–1119 (2015).
- 838 83. Collins, C., Denisin, A. K., Pruitt, B. L. & Nelson, W. J. Changes in E-cadherin rigidity
839 sensing regulate cell adhesion. *Proc. Natl. Acad. Sci.* **114**, E5835–E5844 (2017).
- 840 84. Gavard, J. *et al.* Journal of Cell Science. *J. Cell Sci.* **113**, 2865–2875 (2004).
- 841 85. Nier, V. *et al.* Inference of Internal Stress in a Cell Monolayer. *Biophys. J.* **110**, 1625–
842 1635 (2016).
- 843 86. Saw, T. B. *et al.* Topological defects in epithelia govern cell death and extrusion.
844 *Nature* **544**, 212–216 (2017).
- 845 87. Ma, X., Bao, J. & Adelstein, R. S. Loss of Cell Adhesion Causes Hydrocephalus in
846 Nonmuscle Myosin II-B–ablated and Mutated Mice. *Mol. Biol. Cell* **18**, 2305–2312
847 (2007).
- 848 88. Ma, X. *et al.* Nonmuscle myosin II exerts tension but does not translocate actin in
849 vertebrate cytokinesis. *Proc. Natl. Acad. Sci. U. S. A.* **109**, 4509–14 (2012).

- 850 89. Yonemura, S., Wada, Y., Watanabe, T., Nagafuchi, A. & Shibata, M. α -Catenin as a
851 tension transducer that induces adherens junction development. *Nat. Cell Biol.* 12,
852 533–542 (2010).
- 853 90. Van Dongen, S. F. M., Maiuri, P., Marie, E., Tribet, C. & Piel, M. Triggering cell
854 adhesion, migration or shape change with a dynamic surface coating. *Adv. Mater.* 25,
855 1687–1691 (2013).
- 856 91. Adams, C. L., Chen, Y. T., Smith, S. J. & Nelson, W. J. Mechanisms of epithelial cell-
857 cell adhesion and cell compaction revealed by high-resolution tracking of E-cadherin-
858 green fluorescent protein. *J. Cell Biol.* 142, 1105–19 (1998).
- 859 92. Benjamin, J. M. et al. AlphaE-catenin regulates actin dynamics independently of
860 cadherin-mediated cell-cell adhesion. *J. Cell Biol.* 189, 339–352 (2010).
- 861 93. Lee, E. et al. Deletion of the cytoplasmic domain of N-cadherin reduces, but does not
862 eliminate, traction force-transmission. *Biochem. Biophys. Res. Commun.* 478, 1640–
863 1646 (2016).
- 864 94. van Dongen, S. F. M., Maiuri, P. & Piel, M. A reagent-based dynamic trigger for cell
865 adhesion, shape change, or cocultures. *Methods Cell Biol.* 120, 171–84 (2014).
- 866 95. Vedula, S. R. K. et al. Epithelial bridges maintain tissue integrity during collective cell
867 migration. *Nat. Mater.* 13, 87–96 (2014).
- 868 96. Nier, V. et al. Inference of Internal Stress in a Cell Monolayer. *Biophys. J.* 110, 1625–
869 1635 (2016).
- 870
- 871
- 872
- 873
- 874
- 875
- 876
- 877

Figure 1

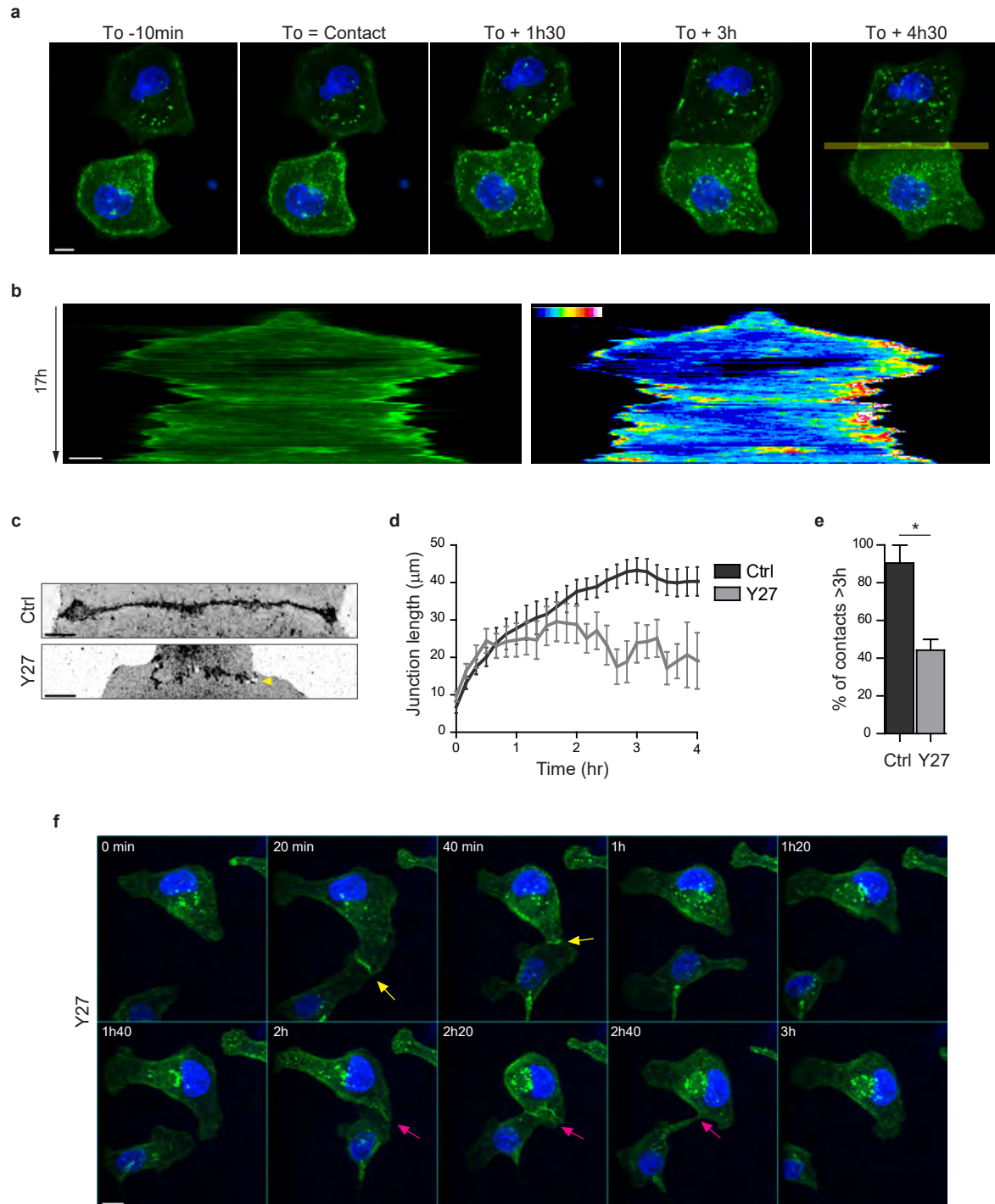


Figure 2

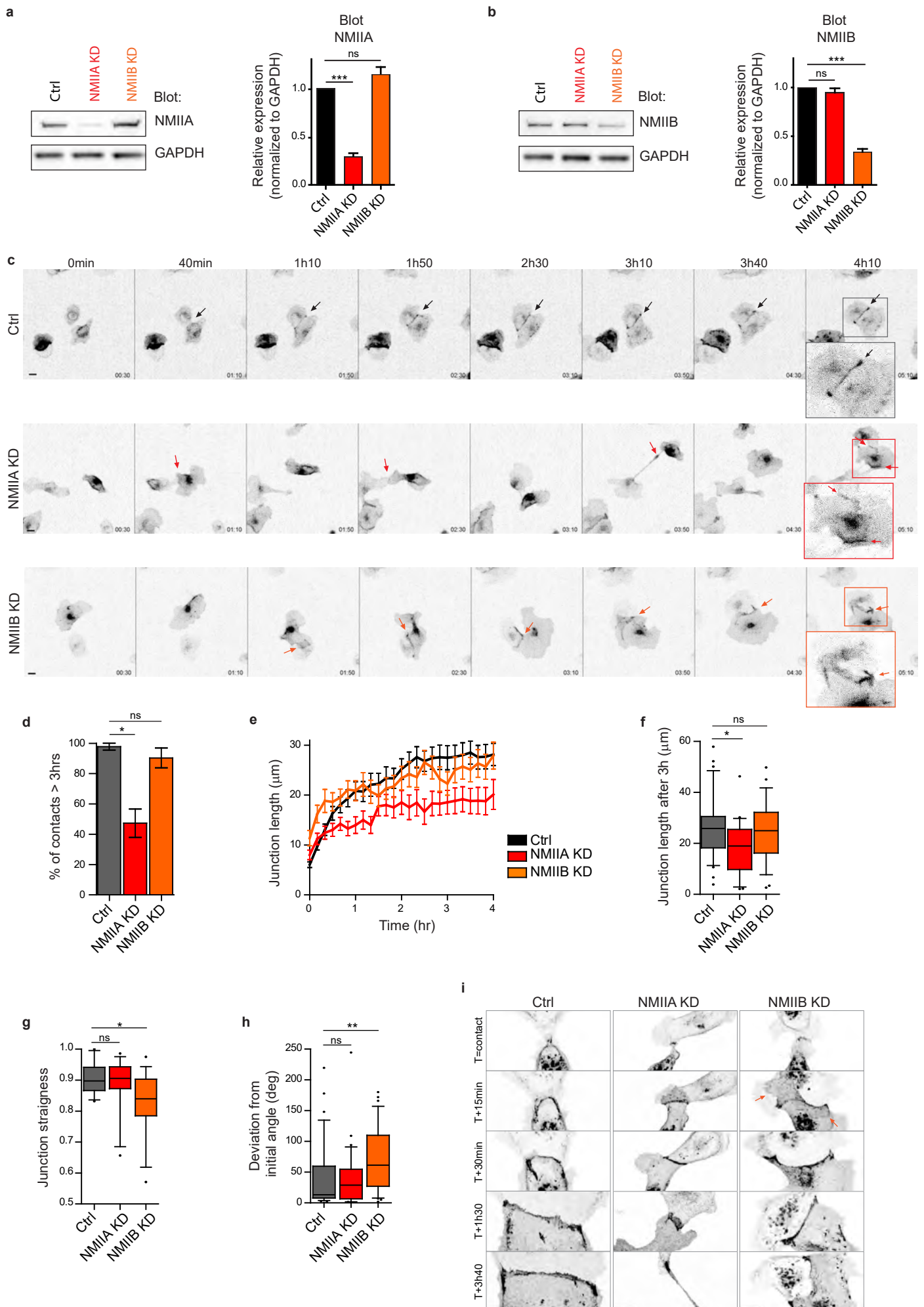


Figure 3

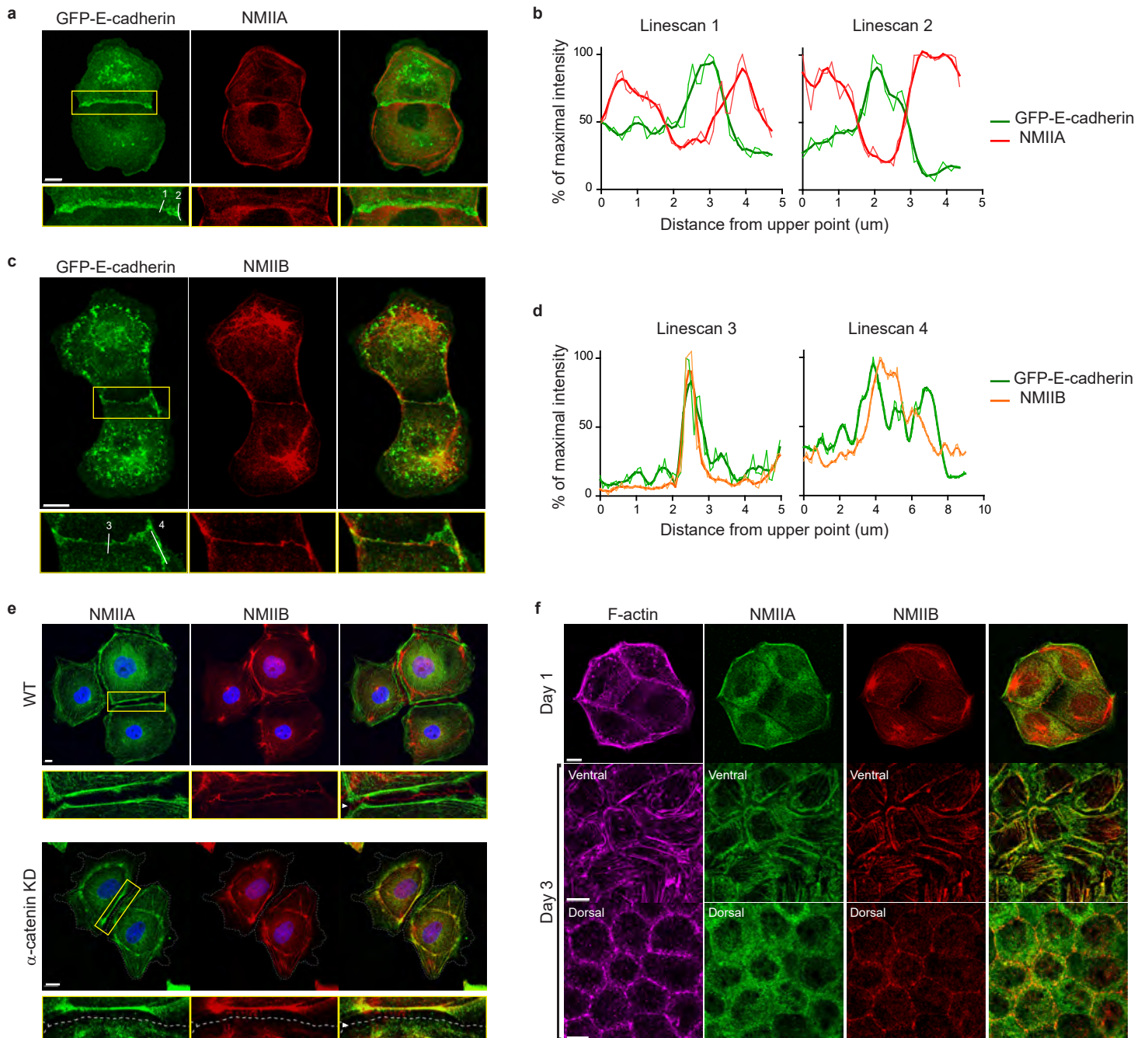


Figure 4

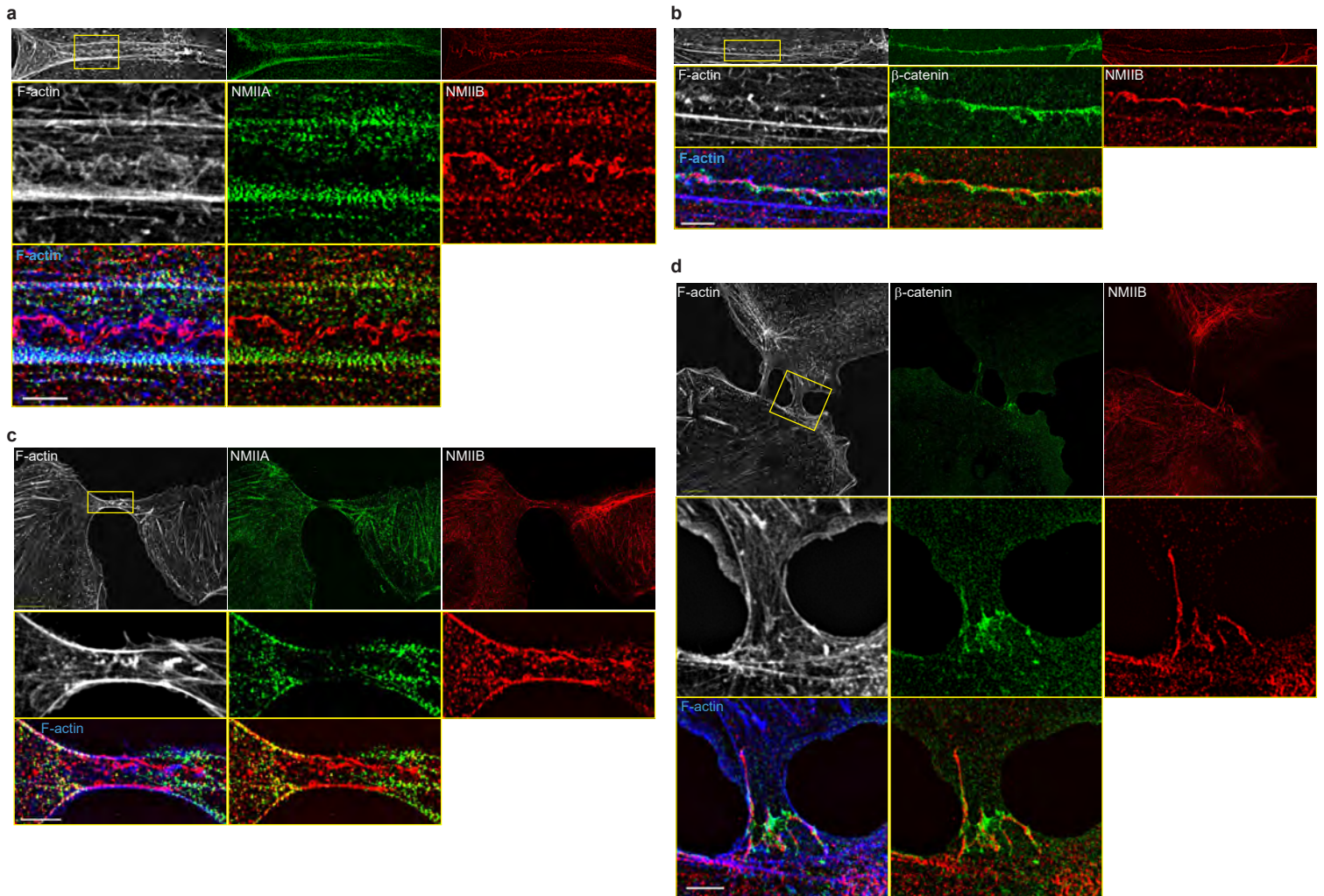


Figure 5

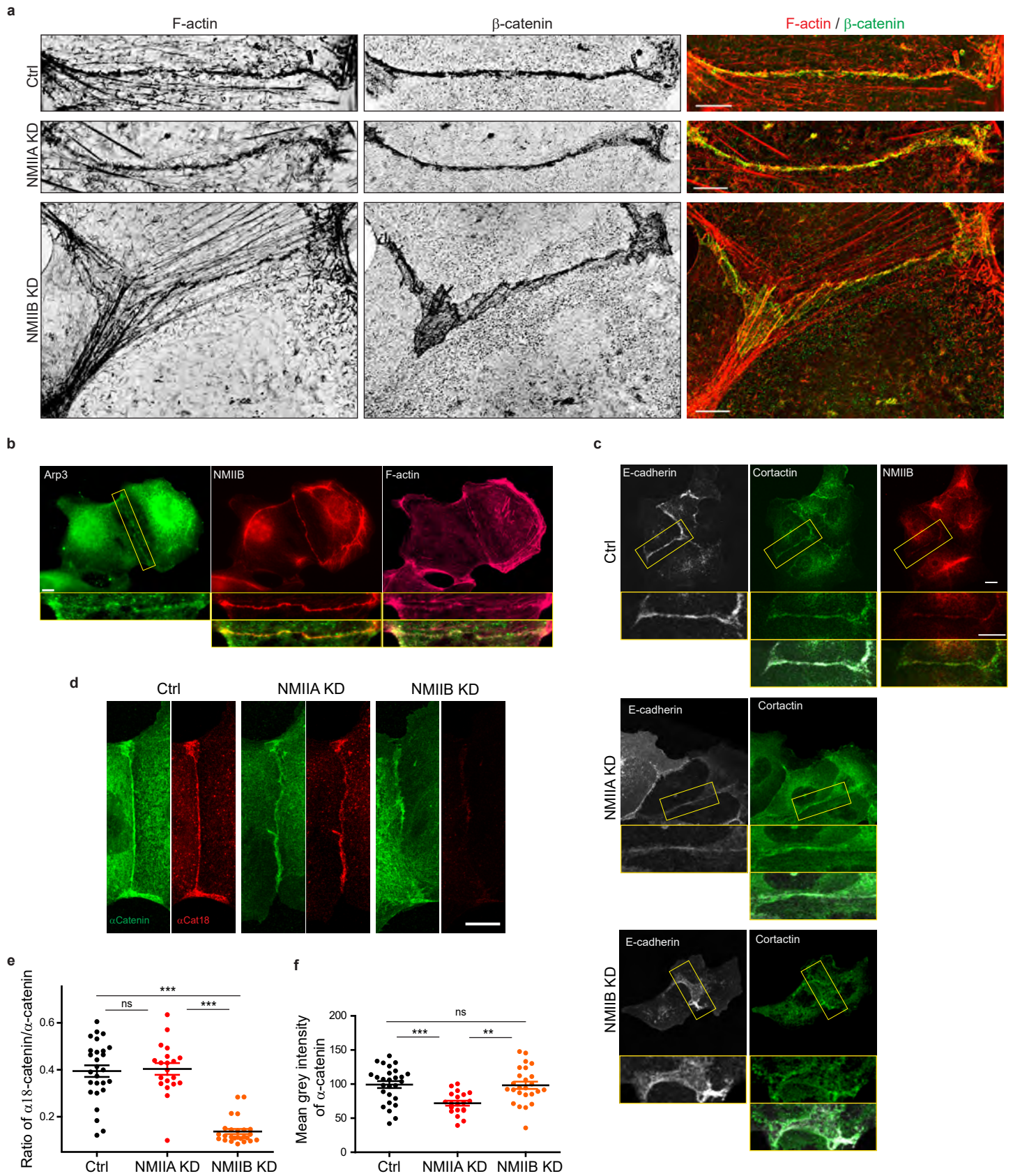


Figure 6

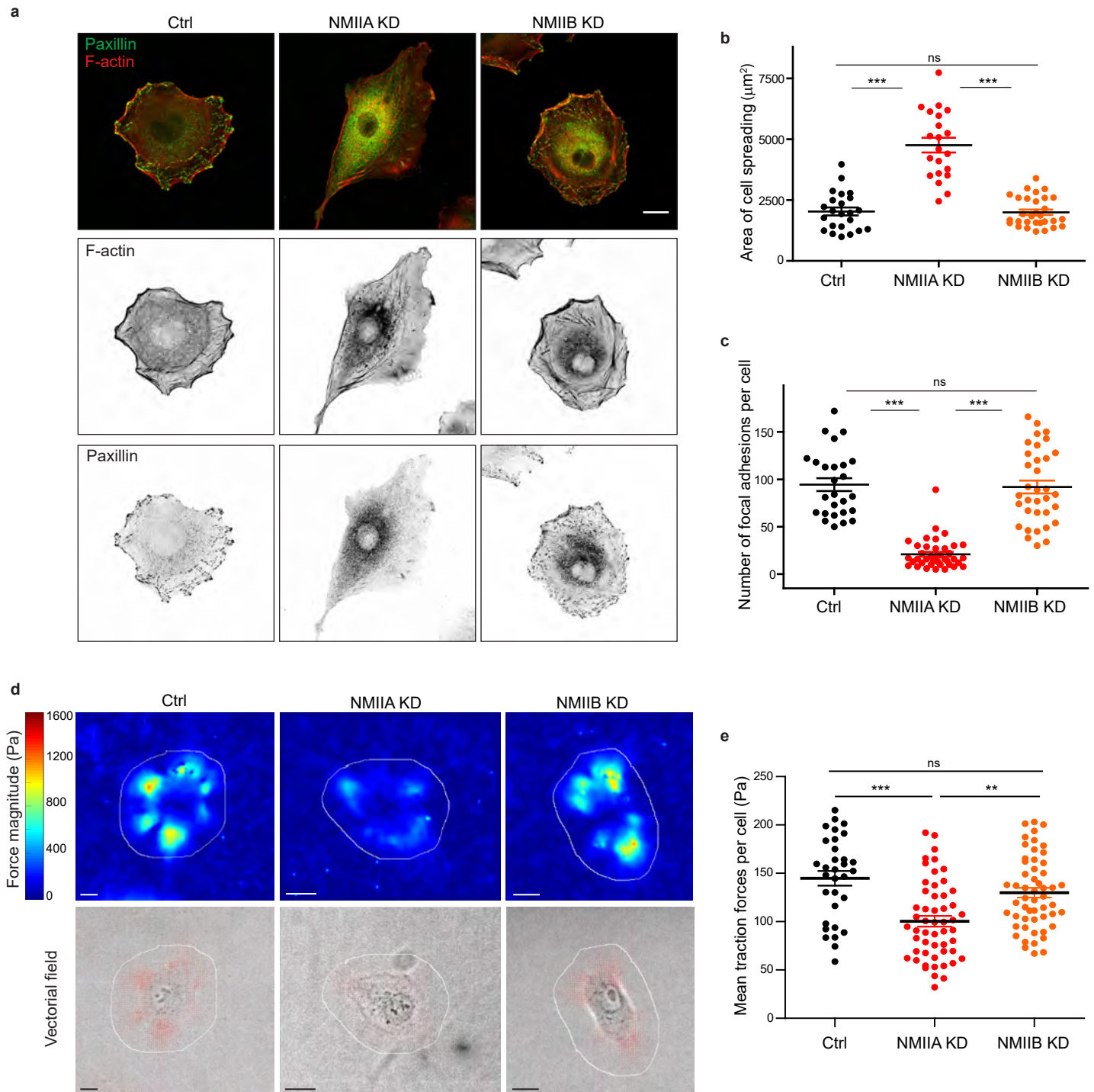


Figure 7

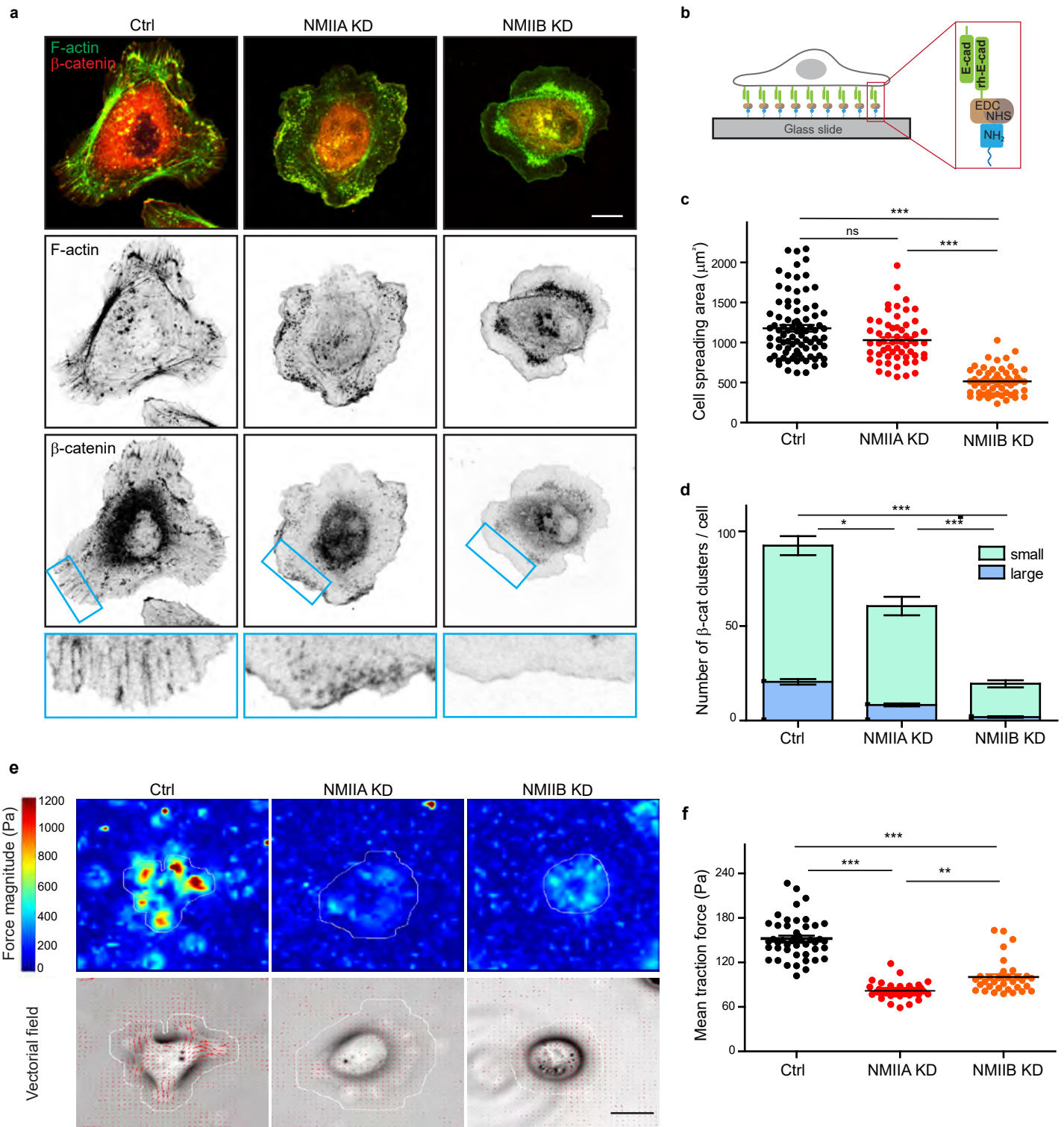
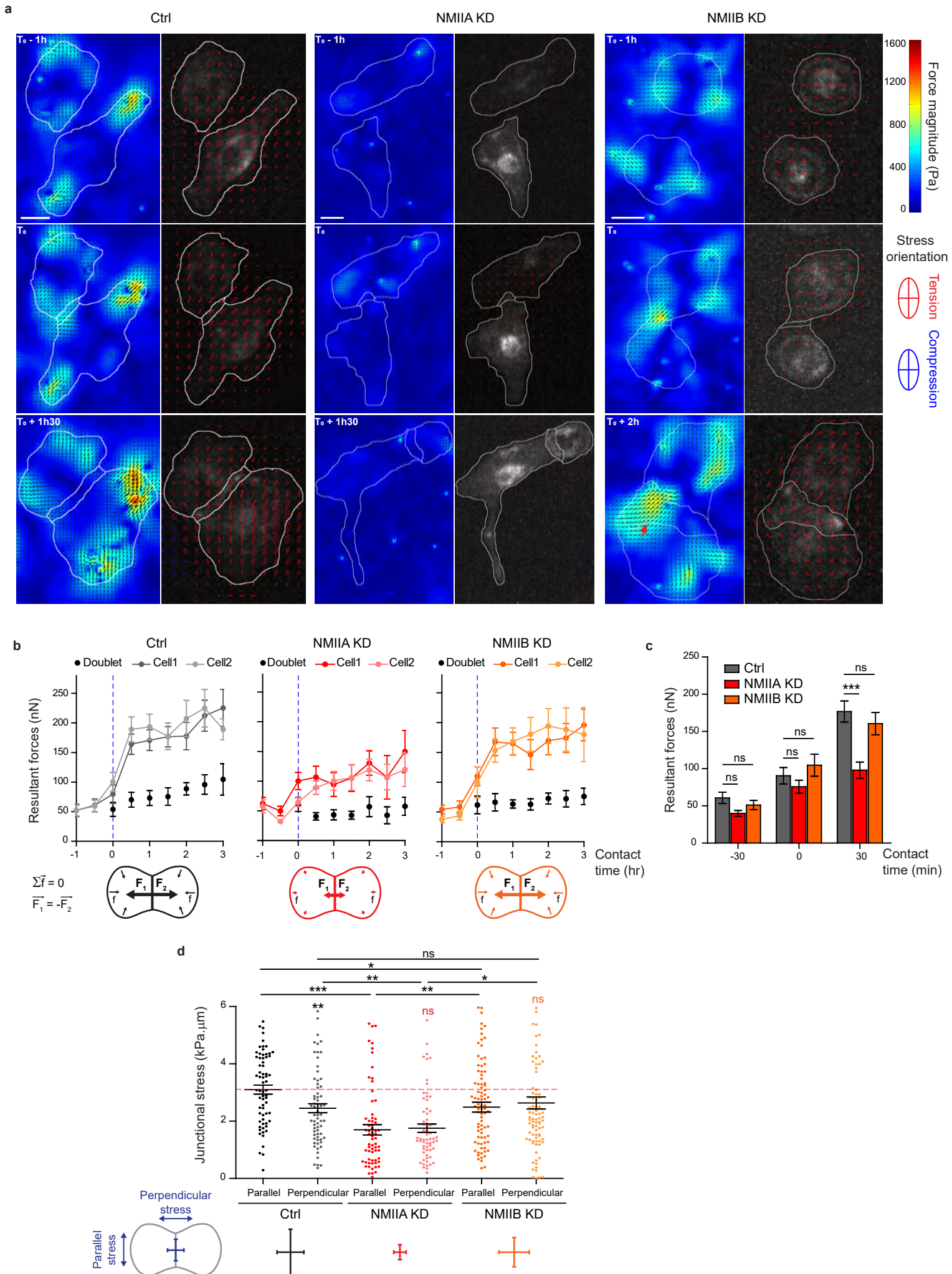


Figure 8



878 **Figure legends**

879

880 **Figure 1: Development of an *in vitro* system for the study of junction biogenesis.**

881 **a.** Spinning disk image sequence showing contact extension between two MDCK cells
882 expressing GFP-E-cadherin and stained with Hoechst. Scale bar: 10 μm . **b.** Kymograph of the
883 junction forming in panel b, generated from the yellow line, shown in green and in pseudocolor
884 to highlight GFP-E-cadherin accumulation at junction tips. The junction axis was realigned
885 horizontally for some time points in order to generate the kymograph on a long time scale.
886 Scale bar: 5 μm . **c.** Representative confocal images of β -catenin-stained junctions from MDCK
887 cell doublets. The arrow points at small holes frequently observed within Y27-treated junctions.
888 The cells were fixed 20 hours after addition of BCN-RGD alone or BCN-RGD + Y27 (50 μM).
889 Scale bar: 10 μm . **d.** Graphs showing the evolution of junction length in function of time after
890 contact initiation in Ctrl and Y27-treated MDCK cell doublets. Y27 (50 μM) was added with
891 BCN-RGD. Data are represented as mean \pm SEM. $n = 13$ and 12 cell doublets from two and
892 three independent experiments, respectively. **e.** Bar graph of the percentage of cell doublets
893 that stay in contact for more than 3 hours in Ctrl and Y27-treated MDCK cells, respectively.
894 Data are represented as mean \pm SEM. $n = 13$ and 12 cell doublets from two and three
895 independent experiments, respectively. Bonferroni statistical tests were applied for p value. **f.**
896 Spinning disk image sequence of GFP-E-cadherin-expressing MDCK cells pre-stained with
897 Hoechst in the presence of Y27 (50 μM). The sequence starts 3 hours after addition of BCN-
898 RGD + Y27. The arrows highlight transient contacts forming under these conditions. Scale bar:
899 10 μm .

900

901 **Figure 2: NMIIA and NMIIB are both required for proper junction biogenesis.**

902 **a.b.** Left panels: Representative immunoblots showing the isoform specific knockdown of
903 NMIIA (a) and NMIIB (b) in NMIIA KD and NMIIB KD MDCK cells. GAPDH expression levels
904 were used as loading controls. Right panels: Bar graphs showing the relative expression level

905 of NMIIA and NMIIB proteins in Ctrl, NMIIA KD and NMIIB KD cells normalized to GAPDH
906 expression levels. Data are represented as mean +/- SEM from three independent
907 experiments. Kruskal-Wallis statistical tests were applied for p value. **c.** Representative
908 epifluorescent image sequences of GFP-E-cadherin over a time course of 5 hours showing the
909 dynamics of junction formation at low magnification in Ctrl, NMIIA KD and NMIIB KD MDCK
910 cells. The arrows indicate the position and the orientation of the junctions. Scale bar: 10 μ m.
911 **d.** Bar graph of the percentage of cell doublets that stay in contact for more than 3 hours. Data
912 are represented as mean +/- SEM. Tukey's multiple comparison statistical tests were applied
913 for p value. n = 36, 37 and 31 cell doublets for Ctrl, NMIIA KD and NMIIB KD cells respectively,
914 from three independent experiments. **e.** Plots showing the evolution of junction length in
915 function of time for Ctrl, NMIIA KD and NMIIB KD cell doublets. Data are represented as mean
916 +/- SEM. n = 40, 43 and 35 cell doublets for Ctrl, NMIIA KD and NMIIB KD cells respectively,
917 from four independent experiments. **f.** Box & whiskers graphs representing the junction length
918 after 3 hours after contact, for Ctrl, NMIIA KD and NMIIB KD cell doublets. n = 34, 21 and 28
919 cell doublets for Ctrl, NMIIA KD and NMIIB KD cells respectively, from four independent
920 experiments. **g.** Box & whiskers graphs showing the junction straightness (calculated as the
921 euclidean/accumulated length ratio) in Ctrl, NMIIA KD and NMIIB KD cell doublets 2 hours
922 after contact. n = 12, 15 and 17 cell doublets for Ctrl, NMIIA KD and NMIIB KD cells
923 respectively, from three independent experiments. **h.** Box & whiskers graph showing the
924 angular deviation of junctions during the 3 first hours of contact in Ctrl, NMIIA KD and NMIIB
925 KD cell doublets. n = 35, 30 and 32 cell doublets for Ctrl, NMIIA KD and NMIIB KD cells
926 respectively, from four independent experiments. **f-h:** Mann-Whitney statistical tests were
927 applied for p value. **i.** Representative spinning disk GFP-E-cadherin image sequences over a
928 time course of 4 hours showing the dynamics of junction formation at high magnification in Ctrl,
929 NMIIA KD and NMIIB KD MDCK cells. The red arrows point at junctional extensions typically
930 observed in NMIIB KD doublets. Scale bar: 10 μ m.

931

932

933 **Figure 3: NMIIB, but not NMIIA, localizes to early AJs**

934 **a.c.** Representative confocal images and zoom boxes of GFP-E-cadherin-expressing MDCK
935 cell doublets fixed 20 h after BCN-RGD addition and immuno-stained for NMIIA (a) or NMIIB
936 (c). Scale bar: 10 μm . **b.d.** Relative intensity profiles (raw and smoothed data) of GFP-E-
937 cadherin and NMIIA (b) or NMIIB (d) signals along the lines represented in (a) and (c)
938 respectively. **e.** Representative confocal images and zoom boxes of WT (upper panel) or α -
939 catenin KD (lower panel) MDCK cells fixed 20 h after BCN-RGD addition and immuno-stained
940 for NMIIA and NMIIB. White arrow heads indicate the cell-cell contact which is depicted as a
941 dotted line in α -catenin KD MDCK cells. Scale bar: 10 μm . **f.** Representative confocal images
942 of WT MDCK cells plated on fibronectin-coated glass for 1 or 3 days and stained for F-actin,
943 NMIIA and NMIIB. Scale bar: 10 μm .

944

945 **Figure 4: NMIIB localizes to a junctional actin network distinct from NMIIA-associated**
946 **actin**

947 **a-d.** SIM (Structured Illumination Microscopy) images of WT MDCK cells fixed 20h after
948 addition of BCN-RGD and stained as indicated. Scale bar: 3 μm .

949

950 **Figure 5: NMIIB supports junctional branched actin organization and regulates α -**
951 **catenin unfolding**

952 **a.** SIM (Structured Illumination Microscopy) images of junctional areas from Ctrl, NMIIA KD
953 and NMIIB KD cells fixed 20 h after addition of BCN-RGD and stained for F-actin and β -catenin.
954 Scale bar: 5 μm . **b.c.** Representative epifluorescent (b) or confocal (c) images with zoom boxes
955 of MDCK cells and stained as indicated. Scale bar: 10 μm . **d.** Representative confocal images
956 of junctional area from Ctrl, NMIIA KD and NMIIB KD cells stained for α -catenin and α -cat18.
957 Scale bar: 10 μm . **e.f.** Scatter plots with mean \pm SEM showing the ratio of junctional α -
958 cat18/ α -catenin signals (e) and the mean intensity levels of α -catenin signal at the junction (f).

959 n = 27, 20, 25 cell doublets for ctrl, NMIIAKD and NMIIBKD, respectively from two independent
960 experiments. Kruskal-Wallis statistical tests were applied for p value.

961

962 **Figure 6: NMIIA, but not NMIIB, regulates cell-matrix adhesions and traction forces**

963 **a.** Representative confocal images of paxillin and F-actin staining of Ctrl, NMIIA KD and NMIIB
964 KD single cells plated on fibronectin-coated glass coverslip for 16 hours. Scale bar: 10 μm .

965 **b.c.** Scatter plots with mean \pm SEM showing the spreading area (b) and number of focal
966 adhesions (c) of Ctrl, NMIIA KD and NMIIB KD single cells plated on fibronectin for 16 hours.

967 n = 23, 21 and 30 cells for (b) and 26, 39 and 34 cells for (c) respectively, from two independent
968 experiments. Kruskal-Wallis statistical tests were applied for p value. **d.** Heat map (upper

969 panel) and vectorial field (lower panel) representing respectively the magnitude and the
970 orientation of traction forces exerted by the single Ctrl, NMIIA KD and NMIIB KD cells, on

971 fibronectin-coated PDMS deformable substrate (30 KPa). Cell masks used for quantification
972 are drawn in white. Scale bar: 10 μm . **e.** Scatter plots with mean \pm SEM showing the mean

973 traction forces exerted by single Ctrl, NMIIA KD and NMIIB KD cells. n = 32, 53 and 54 cells,
974 respectively. Kruskal-Wallis statistical tests were applied for p value.

975

976 **Figure 7: NMIIB favours E-cadherin clustering on E-cadherin-coated substrate**

977 **a.** Confocal images with zoom boxes of Ctrl, NMIIA KD and NMIIB KD cells plated on E-
978 cadherin-coated glass for 6 hours and immuno-stained for β -catenin and F-actin. Scale bar:

979 10 μm . **b.** Scheme depicting the experimental set-up. **c.** Scatter plots with mean \pm SEM
980 showing the cell spreading area of Ctrl, NMIIA KD and NMIIB KD cells plated on E-cadherin

981 coated glass after 6 hours. n = 87, 58 and 58 cells respectively from two independent
982 experiments. Kruskal-Wallis statistical tests were applied for p value. **d.** Bar graph showing the

983 number of β -catenin clusters per cell in Ctrl, NMIIA KD and NMIIB KD cells plated on E-
984 cadherin coated glass. The clusters were classified in two categories: large clusters with area

985 larger than 1 μm^2 , and small clusters with area ranging from 0.2 μm^2 to 1 μm^2 . Data are
986 represented as mean \pm SEM, n = 26, 27 and 26 cells respectively from two independent

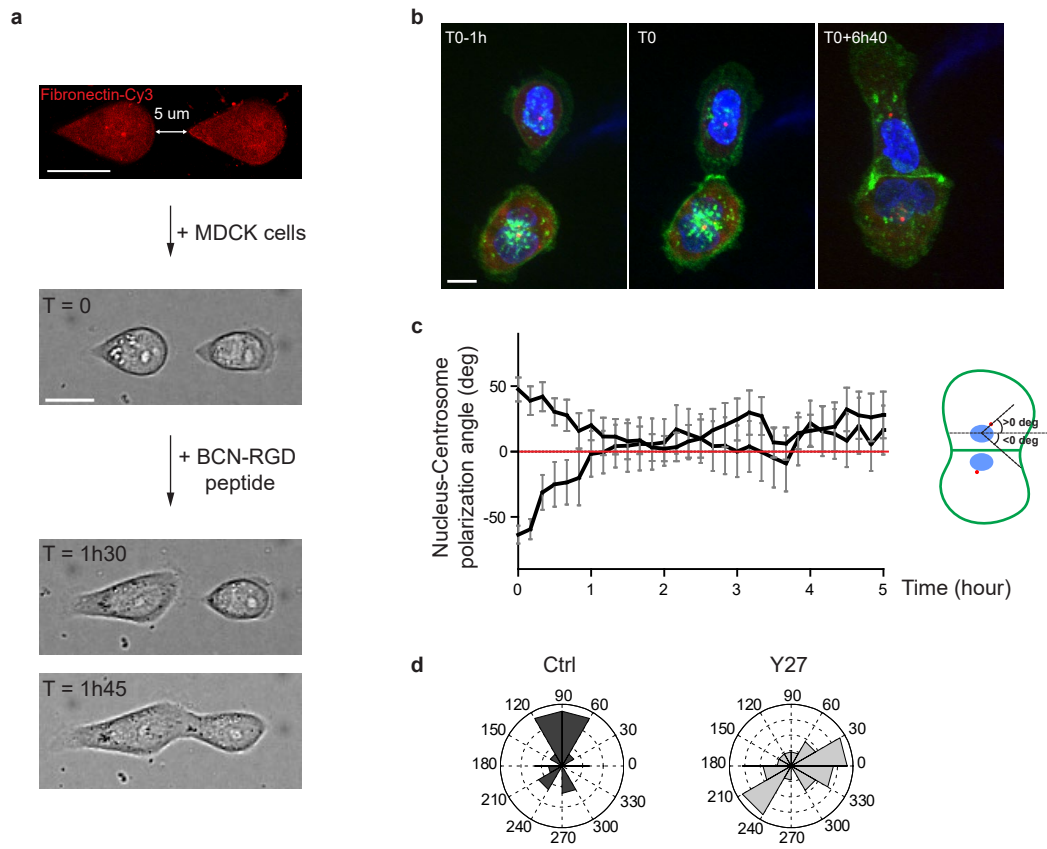
987 experiments. Kruskal-Wallis statistical test were applied for p value **e**. Heat map (top panel)
988 and vectorial field (bottom panel) representing respectively the magnitude and the orientation
989 of traction forces exerted by the single Ctrl, NMIIA KD and NMIIB KD cells on E-cadherin
990 coated PDMS deformable gels (15 KPa). Cell masks used for quantification are drawn in white.
991 Scale bar: 20 μm . **f**. Scatter plots with mean \pm SEM showing the mean traction forces exerted
992 by Ctrl, NMIIA KD and NMIIB KD cells on E-cadherin coated PDMS deformable gels (15 KPa).
993 $n = 46, 34$ and 34 cells respectively from two independent experiments. Kruskal-Wallis
994 statistical tests were applied for p value.

995

996 **Figure 8: NMIIA and NMIIB are both required for establishment of proper inter-cellular**
997 **stress**

998 **a**. Heatmap with vectorial field of traction forces (left panels) and ellipse representation of intra-
999 cellular stress (right panel, the two axes represent the direction and magnitude of the principal
1000 components of the stress tensor, positive values in red, negative values in blue) of inter-cellular
1001 stress (right panels) in Ctrl, NMIIA KD and NMIIB KD cell pairs before, during and after contact
1002 on fibronectin-coated PDMS deformable substrate (30 KPa). Cell contours are drawn in white.
1003 The red arrows indicate a hotspot of traction forces observed frequently in NMIIB KD cell
1004 doublets. Scale bar: 10 μm . **b**. Linear graphs representing the resultant forces of cell doublets
1005 and individual cells before, during and after contact in Ctrl, NMIIA KD and NMIIB KD. Data are
1006 represented as mean \pm SEM. **c**. The same data as in b were represented as bar graph with
1007 mean \pm SEM for statistical comparisons between Ctrl, NMIIA KD and NMIIB KD cells 30
1008 minutes before, during and 30 minutes after contact. Bonferroni statistical tests were applied
1009 for p value. **d**. Scatter plots with mean \pm SEM representing inter-cellular stress in the
1010 junctional area in Ctrl, NMIIA KD and NMIIB KD cells within the first 3 hours of contact. The
1011 stress orientation was divided in the parallel and perpendicular components relative to the main
1012 axis of the junction. Mann-Whitney (for intra-group comparisons) and Kruskal-wallis statistical
1013 tests were applied for p value. **b-d**: $n = 15, 20$ and 18 cell doublets for Ctrl, NMIIA KD and
1014 NMIIB KD, respectively.

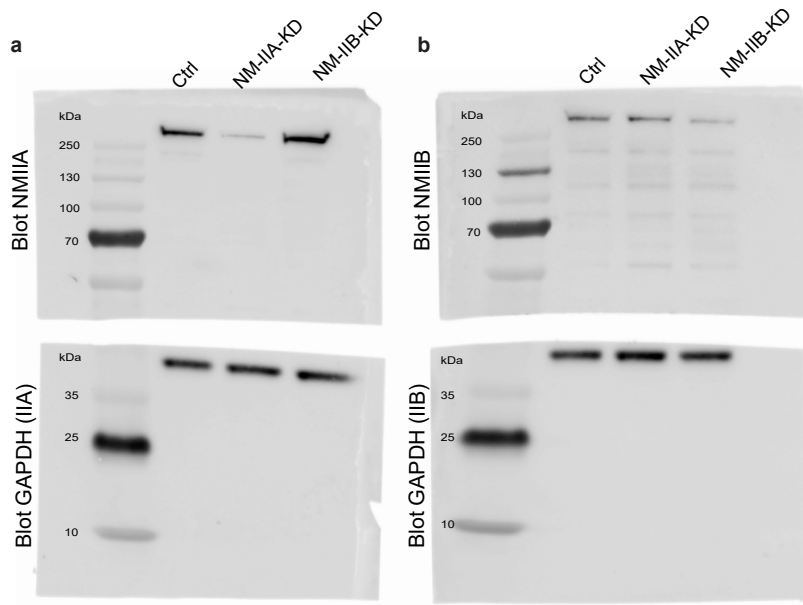
Supplementary Figure 1



Supplementary figure 1: Reversal of nucleus-centrosome polarity axis after cell-cell contact

a. Sequential steps for controlled initiation and visualization of junction biogenesis. The two cells are initially confined on a pair of fibronectin-coated 5 μm -away patterns (T=0). When desired, the cell confinement is released by addition of BCN-RGD peptide, inducing cell spreading and kissing within a few hours. Scale Bar: 10 μm . **b.** Spinning disk image sequence of GFP-E-cadherin and RFP-Pericentrin of doubled transfected MDCK cells pre-stained with Hoechst. Scale bar: 10 μm . **c.** Plots of nucleus-centrosome axis polarization angle relative to junction axis after cell-cell contact. Data are represented as mean \pm SEM. $n = 19$ doublets from three independent experiments. **d.** Distribution of nucleus-centrosome axis polarization angles relative to junction axis after cell-cell contact in Ctrl or Y27-treated MDCK cells at the time when junctions reach their maximal length. $n = 15$ and 21 cells from three and two independent experiments respectively.

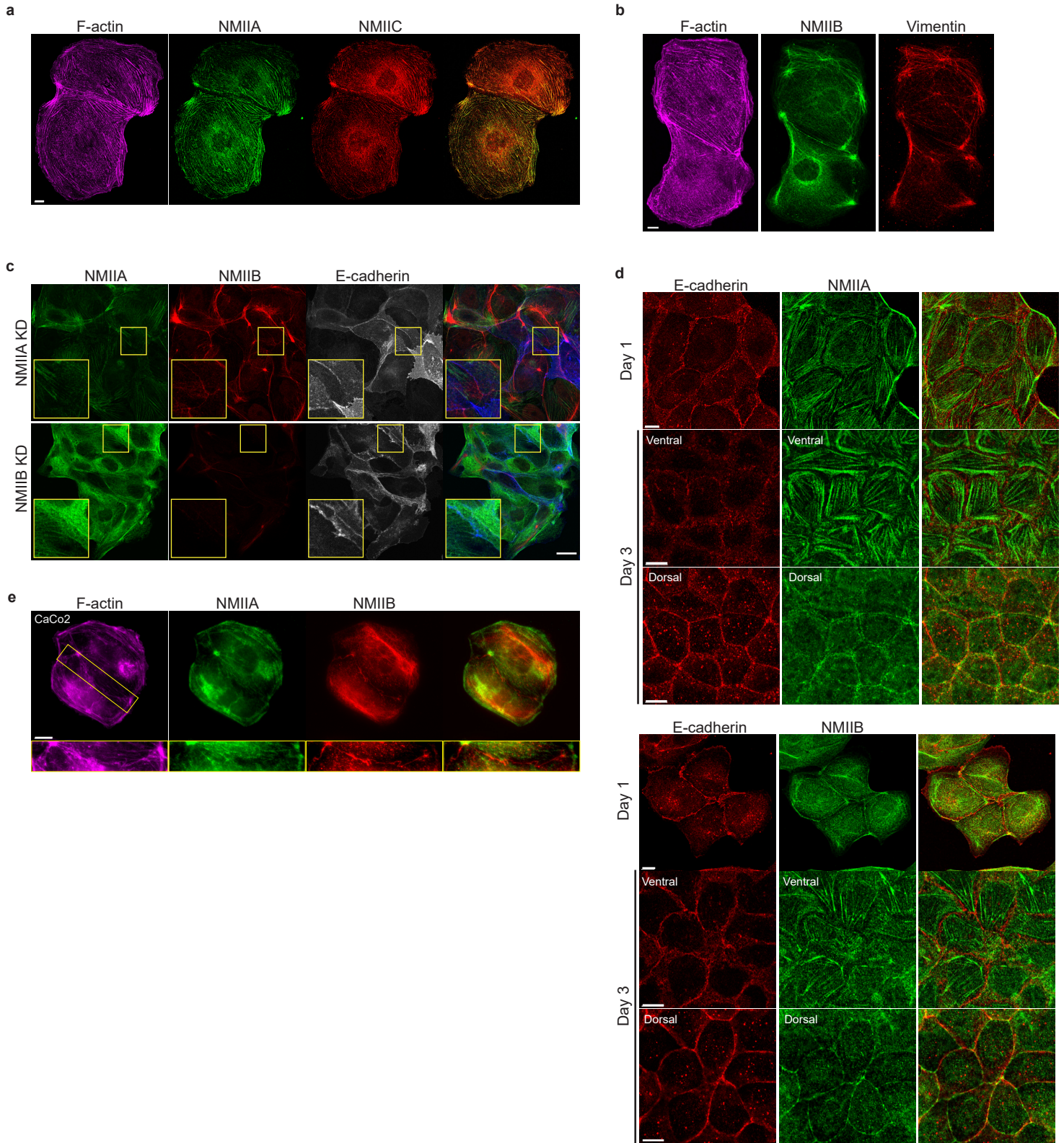
Supplementary Figure 2



Supplementary figure 2: Isoform-specific NMII Knock-down in MDCK cells

a.b. Original uncropped Immunoblots presented in Figure 2a (a) and 2b (b).

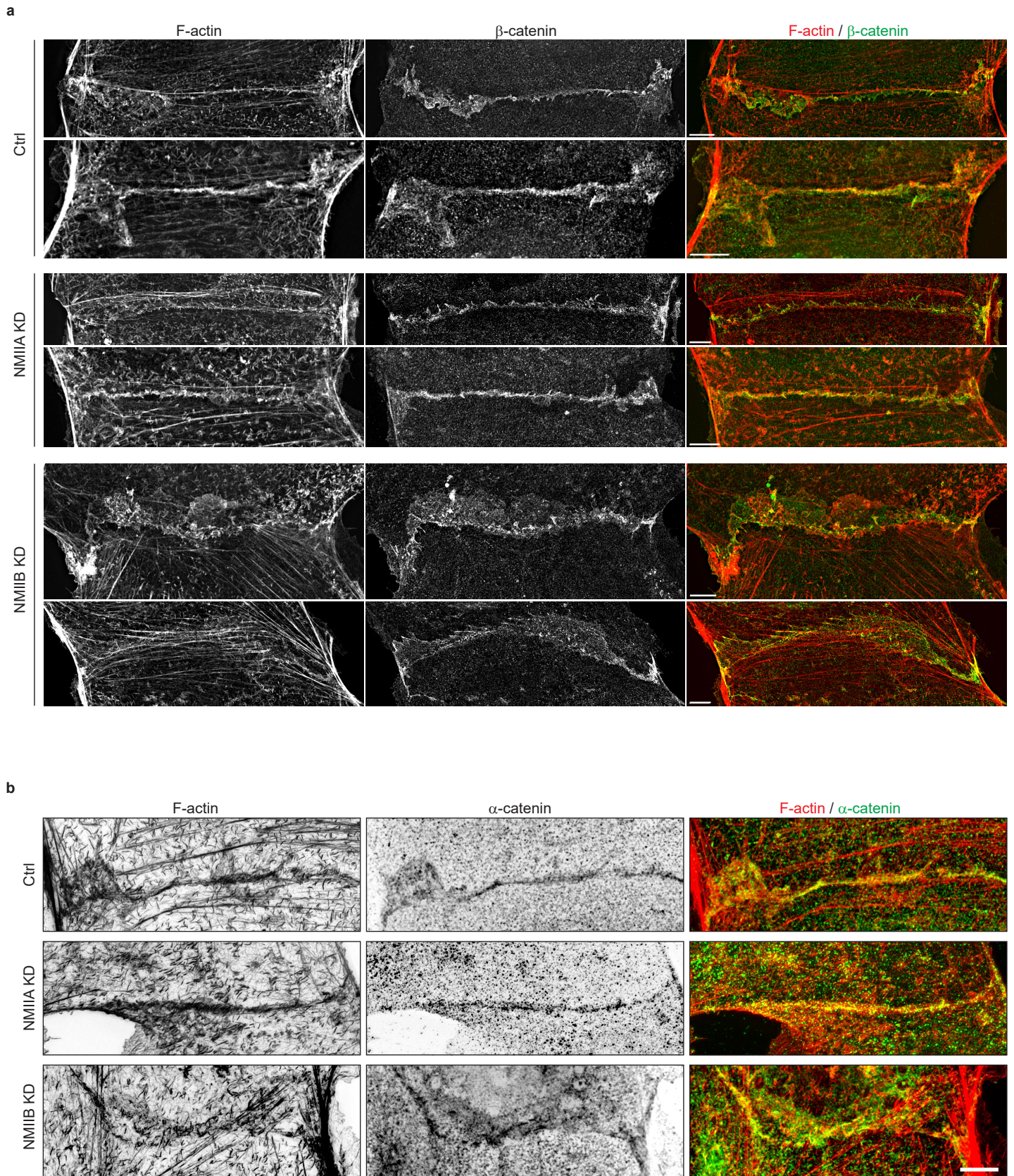
Supplementary Figure 3



Supplementary figure 3: NMIIB, but not NMIIA, localizes to early epithelial AJs

a.b. Representative confocal images of MDCK cell doublets fixed 20h after BCN-RGD addition and stained for F-actin, NMIIA and NMIIC (a) or F-actin, NMIIB and Vimentin (b) as indicated. Scale bar: 10 μ m. **c.** Representative confocal images of NMIIA KD and NMIIB KD MDCK cells plated at low density on fibronectin, fixed after 12 hours and immuno-stained for NMIIA, NMIIB and E-cadherin. Scale bar: 20 μ m. **d.** Representative confocal images of WT MDCK cells plated on fibronectin-coated glass for 1 or 3 days and immuno-stained for E-cadherin and NMIIA (left panel) or NMIIB (right panel). Scale bar: 10 μ m. **e.** Representative epifluorescent images of Caco-2 cells plated at low density on fibronectin, fixed after 12 hours and stained for indicated proteins. Scale bar: 10 μ m.

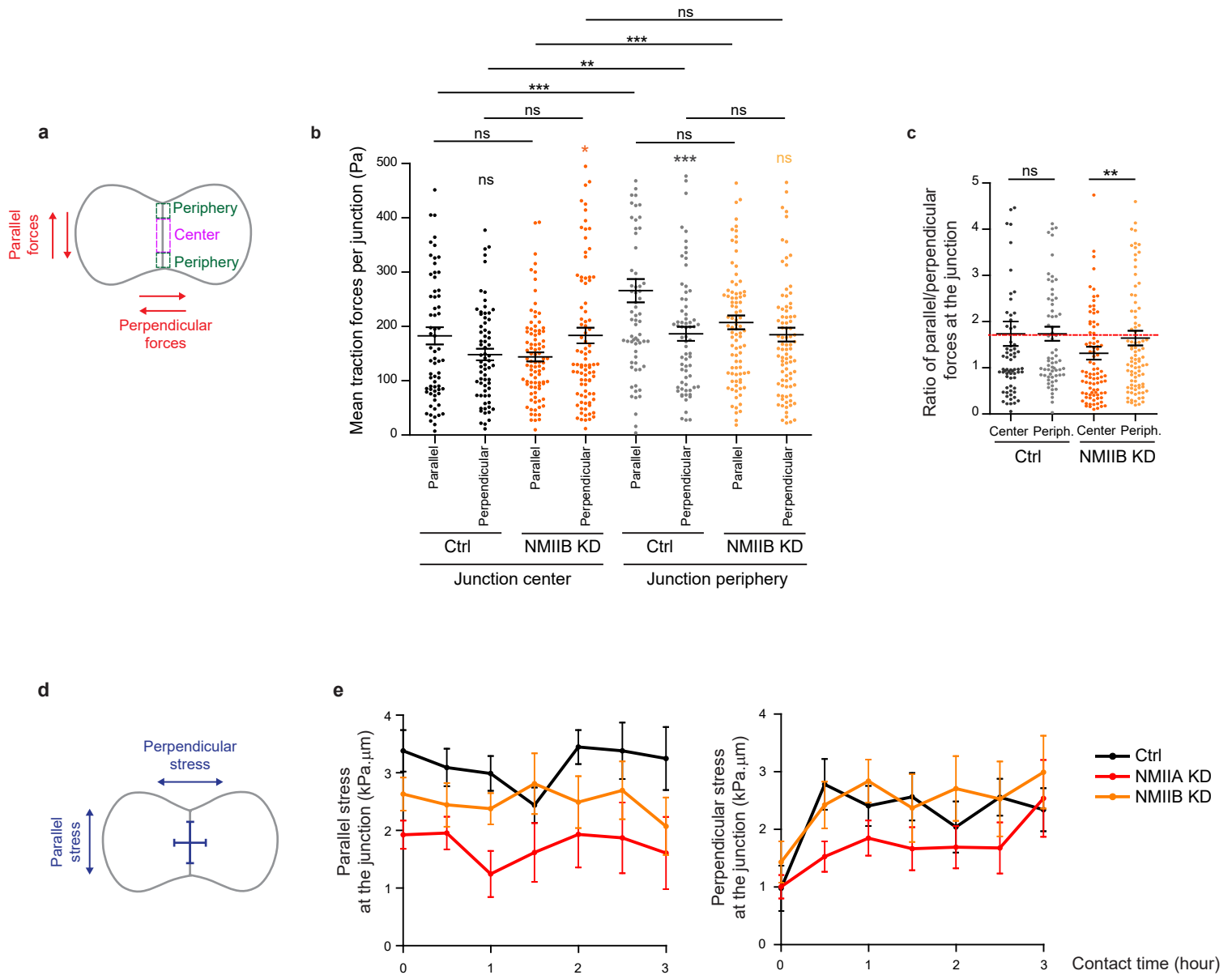
Supplementary Figure 4



Supplementary figure 4: NMIIB supports junctional actin organization

Related to Figure 5a: other examples of junctional actin organization in Ctrl, NMIIA KD and NMIIB KD cells. **a.b.** SIM (Structured Illumination Microscopy) images of junctional area from Ctrl, NMIIA KD and NMIIB KD cells fixed 20h after addition of BCN-RGD and stained for F-actin and β -catenin (a) or α -catenin (b). Scale bar: 5 μ m.

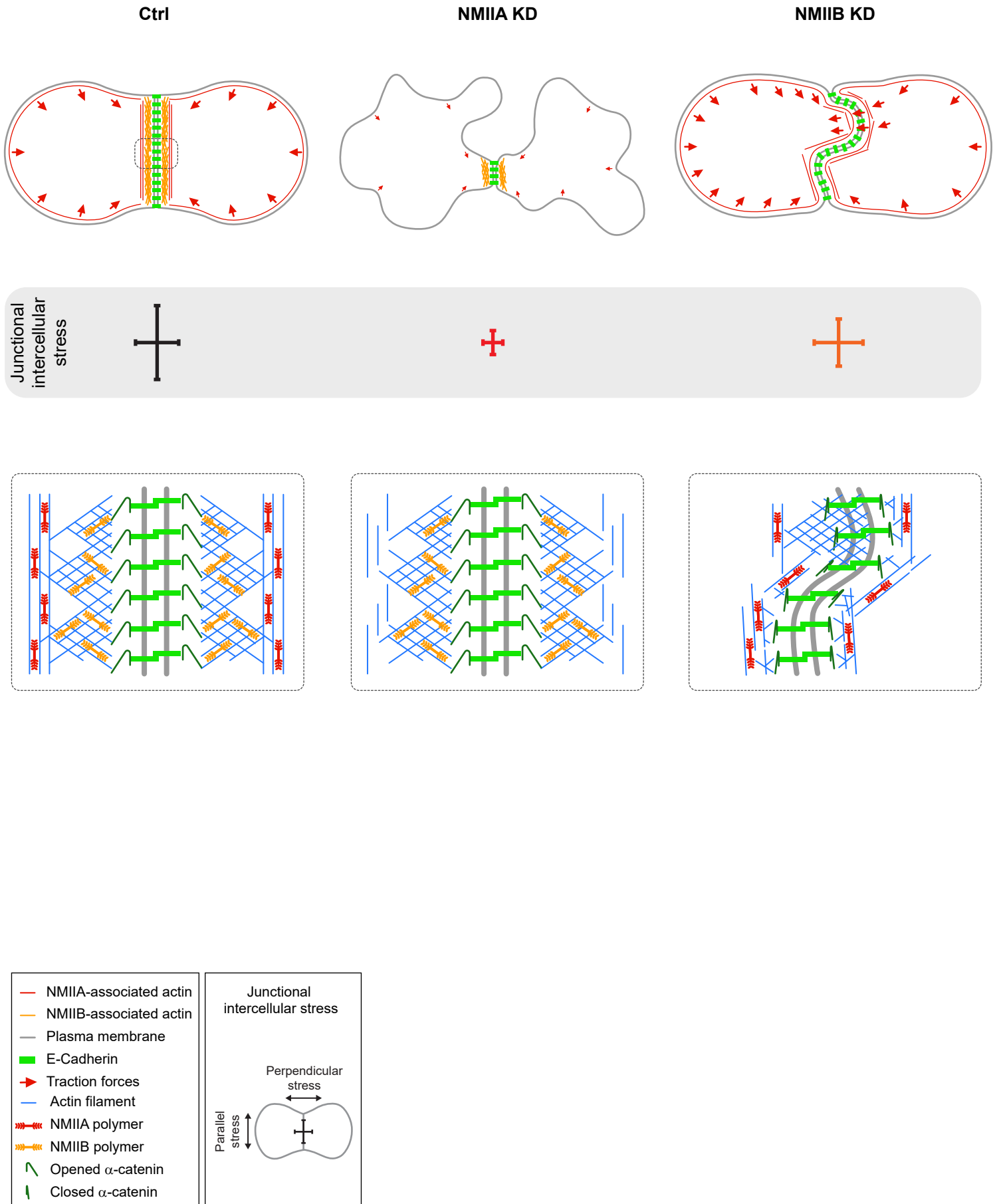
Supplementary Figure 5



Supplementary figure 5: NMIIA and NMIIB are both required for establishment of proper inter-cellular stress

a. Scheme depicting the junction subdomains and the orientation of traction forces relative to the junction axis quantified in (b) and (c). **b.c.** Scatter plots with mean \pm SEM representing the orientation of mean traction forces (b) and the ratio of parallel/perpendicular traction forces (c) in subdomains of the junction in Ctrl and NMIIB KD cells within the first 3 hours of contact. Mann-Whitney (for intra-group comparisons) and Kruskal-wallis statistical tests were applied for p value. n = 15 and 18 cell doublets respectively. **d.** Scheme depicting the orientation of inter-cellular stress relative to the junction axis quantified in (e). **e.** Linear graph of parallel (left panel) and perpendicular (right panel) inter-cellular stress at the junction within the first 3 hours after contact in Ctrl, NMIIA KD and NMIIB KD cells. Data are represented as mean \pm SEM. n= 15, 20 and 18 cell doublets for Ctrl, NMIIA KD and NMIIB KD respectively.

Supplementary Figure 6



Supplementary figure 6: Proposed model for the role of NMIIA and NMIIB during junction biogenesis

Upper panels: summary of the phenotypes observed in Ctrl, NMIIA KD and NMIIB KD cells during junction biogenesis. Lower panels: proposed molecular organization of early junctions in all three cell lines, based on the results obtained in this study and previous ones (see Discussion part).

Ctrl cells establish stable and straight junctions with traction forces mainly peripheral, generating an anisotropic intercellular stress preferentially parallel to the junction. NMIIB associates to- and organizes the junctional branched actin meshwork, and favours the opening of α -catenin molecules. NMIIA, which provides mechanical tugging force, sits on distant perijunctional actin bundles parallel to the junction. Actin cables parallel to the cortex and ventral stress fibers (not represented here for clarity of the figure).

NMIIA KD cells fail to keep contact for long times, exhibit shorter junctions, weak traction forces and weak intercellular stress. Perijunctional actin bundles are smaller and disorganized. The junctional NMIIB-actin meshwork still supports α -catenin opened conformation but it does not prevent the junction from disassembly.

NMIIB KD cells establish persistent but wavy junctions from which lamellipodial extensions and traction force hotspots arise. There is no preferential orientation of intercellular stress. The junctional branched actin meshwork is disorganized, which probably prevents α -catenin opening and induces the formation of lamellipodial extensions. The anchoring of perijunctional actin bundles to the junction is perturbed, despite the presence of NMIIA.

Supplementary Video legends

Supplementary Video 1: Dynamic of junction formation on reversible micropatterns

Spinning disk movie showing contact formation between two MDCK cells expressing GFP-E-cadherin and stained with Hoechst. Scale bar: 10 μm .

Supplementary Video 2: Dynamic of junction formation in Y27-treated cells

Spinning disk movie of MDCK cells expressing GFP-E-cadherin, stained with Hoechst and treated with 50 μM Y27. Scale bar: 10 μm .

Supplementary Video 3: Dynamic of junction formation in Ctrl, NMIIA KD and NMIIB KD cells

Epi-fluorescent movies of Ctrl, NMIIA KD and NMIIB KD MDCK cells expressing GFP-E-cadherin. Scale bar: 10 μm .